
A Recursive Bayesian Neural Network for Constitutive Modeling of Sands under Monotonic and Cyclic Loading

Toiba Noor

Department of Civil Engineering
Indian Institute of Technology Delhi
cez217542@iitd.ac.in

Soban Nasir Lone

Department of Transportation Systems Engineering
Technical University of Munich
soban.lone@tum.de

G. V. Ramana

Department of Civil Engineering
Indian Institute of Technology Delhi
ramana@civil.iitd.ac.in

Rajdip Nayek

Department of Applied Mechanics
Indian Institute of Technology Delhi
rajdipn@am.iitd.ac.in

ABSTRACT

In geotechnical engineering, constitutive models are central to capturing soil behavior across diverse drainage conditions, stress paths, and loading histories. While data-driven deep learning (DL) approaches have shown promise as alternatives to traditional constitutive formulations, their practical deployment requires models that are not only accurate but also capable of quantifying predictive uncertainty. This study introduces a recursive Bayesian neural network (rBNN) framework that unifies temporal sequence learning with generalized Bayesian inference to achieve both predictive accuracy and rigorous uncertainty quantification. A key innovation is the incorporation of a sliding-window recursive structure that enables the model to effectively capture path-dependent soil responses under monotonic and cyclic loading. By treating network parameters as random variables and inferring their posterior distributions via generalized variational inference, the rBNN produces well-calibrated confidence intervals alongside point predictions.

The framework is validated against four datasets spanning both simulated and experimental triaxial tests: monotonic loading using a Hardening Soil model simulation and 28 consolidated drained (CD) tests on Baskarp sand, and cyclic loading using an exponential constitutive simulation of CD/CU tests and 37 experimental cyclic CU tests on Ottawa F65 sand. This structured progression—from monotonic to cyclic and from simulated to experimental data—demonstrates the robustness and adaptability of the proposed approach across varying levels of data fidelity and complexity.

Comparative analyses with LSTM, Encoder–Decoder, and GRU architectures highlight that rBNN not only achieves competitive predictive accuracy but also provides reliable confidence intervals, thereby offering a balanced integration of accuracy and interpretability. By directly addressing the challenges of cyclic soil behavior with a probabilistic, temporally aware architecture, this work advances the frontier of data-driven constitutive modeling in geotechnical engineering.

Keywords Sand Constitutive Modeling; Deep Learning; Recursive Neural Network; Bayesian Modeling; Generalized Variational Inference

1 Introduction

Constitutive modeling enables prediction of soil response under diverse drainage conditions, stress paths, and loading histories. Unlike metals, soils — particularly sands — exhibit nonlinear, path-dependent behavior due to their granular structure, density, and stress history [1, 2]. Accurate models are essential for designing and safety assessment of foundations, tunnels, offshore structures, and landslide-prone slopes [3, 4, 5, 6].

Traditional constitutive models — including elastic, viscoelastic, elastoplastic, and micromechanical formulations describe features such as hardening, dilatancy, and pore pressure evolution [7, 8, 9, 10, 11, 12, 13]. However, they demand extensive parameter calibration, offer limited generalization, and may suffer from numerical instability [14, 15]. These limitations are acute for sands, which display dilatancy [16], state dependence [17], and anisotropy [18], especially under cyclic loading. Capturing these behaviors accurately often necessitates highly specialized and data-intensive constitutive formulations, which can be cumbersome in practice.

To overcome these limitations, data-driven approaches, especially deep learning (DL) techniques, have emerged as promising alternatives. They learn stress–strain relationships directly from data, bypassing explicit formulations and extensive parameter calibration. Early applications used feedforward neural networks (FFNNs) to model monotonic loading [19, 20, 21, 22, 23, 24] (see Fig. 1a). However, FFNNs are static and accumulate error during sequential prediction. Recursive FFNNs (rFFNNs) address this by incorporating their own predictions into subsequent inputs (see Fig. 1b)[25, 26]. Typically, as described in literature, rFFNNs are trained to predict the *entire series* from the initial stress value *all at once*, aligning the training process with the prediction strategy. While theoretically superior, in practice this often causes error accumulation: small inaccuracies at early steps propagate and amplify. Especially producing phase shifts and amplitude errors in cyclic loading [27]. Although the loss averages over all steps, early errors are hard to correct since gradients diminish or destabilize through many recursions [28, 29].

In the current study, we propose a revised training strategy for rFFNNs based on multiple overlapping sliding windows with varying starting points. The full loading sequence is divided into shorter, fixed-length windows, each of which recursively combines its own predictions with inputs, mimicking the inference procedure but over a limited horizon. This constrains recursion depth, improves gradient flow, and allows localized error correction. The window length acts as a tunable hyperparameter that balances temporal context with training stability. Inference remains autoregressive over the full sequence, but training becomes more stable and computationally efficient, improving accuracy, especially, in nonlinear cyclic stress–strain modeling of sand.

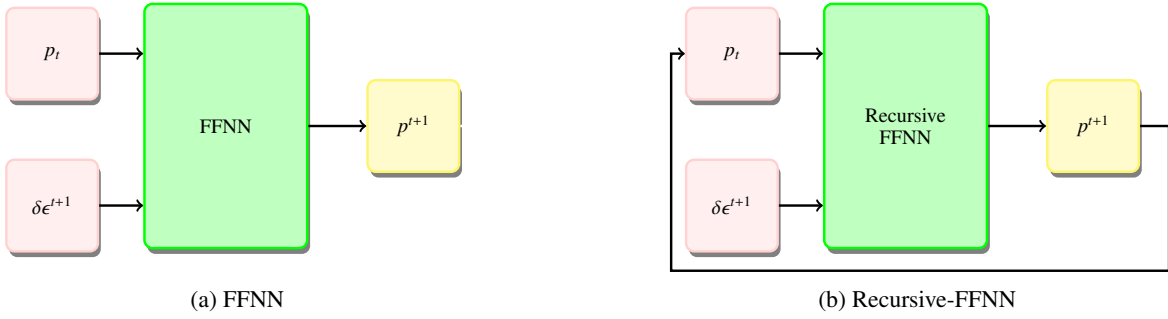


Figure 1: Comparison of FFNN and rFFNN training approach: (a) A single-step FFNN utilizes the measured current stress state and strain increment to predict the subsequent stress state. (b) The rFFNN incorporates the predicted stress state from the current step as feedback to predict the next stress state, recursively incorporating prior predictions as inputs to capture sequential and path-dependent stress-strain behavior.

While this work focuses on improving rFFNNs with a sliding window strategy, it is important to contrast with recent alternatives such as recurrent neural networks (RNNs), Long Short-Term Memory (LSTM), and Gated Recurrent Units (GRUs), widely applied in sequential modeling. RNNs naturally advanced sand constitutive modeling by maintaining memory over multiple load steps by summarizing previous information through "hidden states", thus capturing temporal dependencies beyond first-order Markov models. However, early RNNs struggled with vanishing and exploding gradients, limiting their ability to represent stress–strain–volume change behavior of granular materials [30, 31, 32]. To overcome these issues, advanced architectures like LSTM [33] and GRU [34] introduced gating mechanisms that regulate information flow, allowing longer memory and mitigating gradient problems. These models have proven effective for capturing complex sand constitutive behavior [35, 36, 37, 38, 39], particularly under cyclic loading where path dependency is critical. Notably, LSTMs and GRUs have demonstrated strong performance in drained and undrained conditions [40], including tasks such as predicting shear strain, excess pore pressure, and liquefaction potential [41, 42].

Encoder–decoder architectures extend recurrent models by separating input encoding from output generation, supporting structured sequence-to-sequence prediction and long-range dependency capture [43, 44]. Here, the encoder is a bidirectional LSTM (BiLSTM) that incorporates information from past and future load steps, while the decoder is a unidirectional LSTM generating outputs in a causal manner. To our knowledge, such an encoder–decoder formulation has not been applied to sand constitutive modeling and is introduced here as a deterministic sequence-to-sequence baseline under comparable training and inference conditions.

While ML and DL models offer attractive alternatives in capturing complex relationships without the need for explicit physical laws, they also present challenges, such as optimizing training techniques, managing limited and noisy data, effectively quantifying uncertainties, and minimizing overfitting risks. These models are generally trained on either simulated or experimental data; simulated data is based on a limited number of simulations, while experimental data tends to be both sparse and noisy. As such, data-driven models must inherently account for the “limited-data uncertainty” for simulated data. For experimental data, uncertainty arises additionally due to modeling and the presence of measurement variability (noisy data uncertainty) in data. Traditional deterministic DL models, including FFNNs, rFFNNs, RNNs, Encoder-Decoder models, and LSTMs, only yield point estimates, failing to quantify the uncertainties inherent in the data. However, implementing uncertainty quantification (UQ) in ML/DL models is also crucial since it provides end-users with confidence bounds that reflect prediction quality and support better-informed decision-making in geotechnical applications.

To overcome these limitations, we enhance the FFNN architecture by incorporating uncertainty modeling, treating the model parameters β as random variables, and introducing a deterministic uncertainty layer as the final layer in the FFNN. By deterministic uncertainty layer, we mean that the output is a distribution (in our case Gaussian distribution), with the mean and standard deviation as a deterministic function of the FFNN parameters. This uncertainty output layer allows us to write a Gaussian distribution over the predictions with an inferred mean and standard deviation. As such, the model parameters β becomes amenable to Bayesian inference, akin to Bayesian neural networks (BNNs) [45, 46, 47]. These random variables, characterized by probability distributions, capture the uncertainty in the parameters. However, as will be explained later in Section 3.2, a recursive loss-based formulation over multiple overlapping sliding windows causes a departure from likelihood-based formulation. Therefore, we adopt a *generalized* Bayesian inference framework, which allows the use of loss function instead of likelihood function [48, 49, 50]. Additionally, Bayesian approaches mitigate overfitting by automatically regularising the models by using a prior distribution as inductive bias. There exists a work in soil constitutive modeling, where BNNs have been applied for the purpose of regularization [51]. Similarly, methods like Monte Carlo (MC) dropout [52], have been used for regularization but can also be used for UQ [53]. However, MC dropout does not provide the comprehensive probabilistic modeling that a fully Bayesian approach offers [52]. A Bayesian paradigm, offers a systematic way of UQ, while also preventing overfitting since they are automatically regularized.

To the best of the authors’ knowledge, this is the first fully Bayesian framework for constitutive modeling of sands by implementing a recursive generalized Bayesian neural network (rBNN). The contributions are: (a) a sliding-window training strategy for rFFNNs, (b) a Bayesian extension with uncertainty-aware predictions, and (c) benchmarking against deterministic sequence models under monotonic and cyclic loading. The remainder of this paper describes the problem setup (Section 2), methodology (Section 3), performance assessment (Section 4), discussion (Section 5), and conclusions (Section 6).

2 Problem Setup

This study aims to develop uncertainty-aware probabilistic constitutive models for sandy soils under quasi-static triaxial loading. Two separate modeling frameworks are proposed, each trained on data from M strain-controlled tests: one for *monotonic* loading under consolidated drained (CD) conditions, and another for *cyclic* loading under consolidated undrained (CU) conditions. The choice aligns with standard geotechnical practice for sands: CD tests characterize strength and volumetric response under drained conditions, while undrained cyclic tests replicate rapid loading scenarios—such as seismic events—where drainage is restricted and excess pore pressure accumulation governs soil instability and liquefaction. These conditions are particularly relevant given the drainage behavior and liquefaction susceptibility of sandy soils.

Each test records the stress-strain-volume (or pore pressure) responses of a sand sample under controlled loading conditions. Initially, the sand sample is consolidated under a constant confining pressure σ_3 , and then incremental compressive axial strains $\delta\epsilon$ are applied through quasi-static loading, illustrated in Fig. 2. These load steps represent pseudo-time indices, allowing the modeling of sequential soil responses. At each load step, the mean effective stress (p) and deviatoric stress (q) are computed as:

$$p = \frac{\sigma_1 + 2\sigma_3}{3}, \quad q = \sigma_1 - \sigma_3 \quad (1)$$

The interpretation of the third state parameter varies with the type of test. In monotonic CD tests, the void ratio e is directly computed from the initial void ratio e_0 and the measured volume change, modified due to the rearrangement of particles. In contrast, cyclic triaxial tests are conducted under undrained conditions, where no volume change occurs; instead, the evolution of pore pressure is tracked through the excess pore pressure ratio r_u . While e and r_u represent fundamentally different physical properties, for ease of algorithmic implementation, a unified notation e is adopted

internally to represent either e or r_u or volumetric strain ϵ_v , depending on the test context. However, to preserve clarity and physical accuracy, all figures and tables retain the original variables.

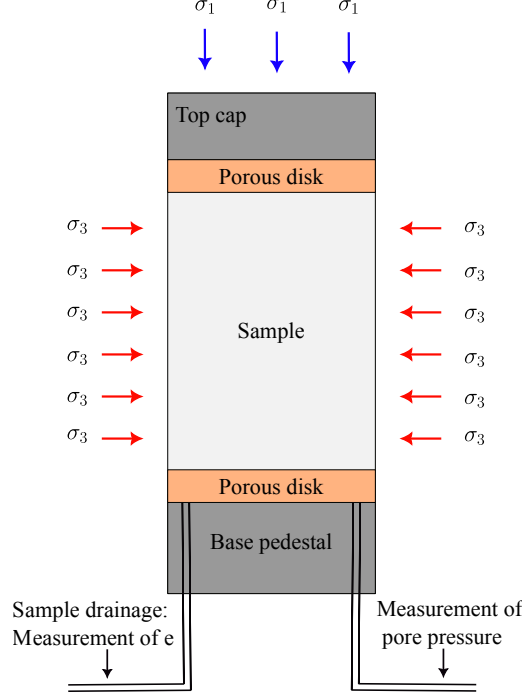


Figure 2: Schematic of the triaxial test setup.

Each triaxial test $m \in \{1, 2, \dots, M\}$ consists of multiple load steps $t \in \{1, \dots, N\}$, with a state vector at each step defined as:

$$\mathbf{s}_t^{(m)} = [p_t^{(m)}, q_t^{(m)}, e_t^{(m)}]^T \quad (2)$$

This state vector characterizes the mechanical behavior of the soil for the m^{th} triaxial test at the t^{th} load step. It is influenced by a set of exogenous inputs $\mathbf{u}_t^{(m)}$, which vary depending on the loading type:

- **Monotonic loading:** $\mathbf{u}_t^{(m)} = \{\epsilon_t^{(m)}, d\epsilon_t^{(m)}\}$
- **Cyclic loading:** $\mathbf{u}_t^{(m)} = \{\epsilon_t^{(m)}, d\epsilon_t^{(m)}, \Delta_t^{(m)}, c_t^{(m)}\}$

Here, $\epsilon_t^{(m)}$ is the axial strain, $d\epsilon_t^{(m)}$ is its increment, $\Delta_t^{(m)} \in \{-1, +1\}$ denotes the strain direction (loading or unloading), and $c_t^{(m)}$ is the current cycle number. Additionally, each test is associated with triaxial test constants $\boldsymbol{\theta}^{(m)} = \{\sigma_3^{(m)}, e_0^{(m)}\}$. The systematic variation of $\boldsymbol{\theta}^{(m)}$ enables the representation of diverse mechanical behaviors of sand samples with the same constitutive properties.

The multiple triaxial tests dataset is represented as follows:

$$\text{Dataset} = \left\{ \boldsymbol{\theta}^{(m)}, \left(\mathbf{s}_0^{(m)}, \mathbf{u}_0^{(m)} \right), \dots, \left(\mathbf{s}_t^{(m)}, \mathbf{u}_t^{(m)} \right), \dots, \left(\mathbf{s}_N^{(m)}, \mathbf{u}_N^{(m)} \right) \right\}_{m=1}^M$$

The goal is to characterize the evolution of soil states through the mapping f_β , where a deterministic framework relates the previous state to the next:

$$\mathbf{s}_t^{(m)} = f_\beta \left(\mathbf{s}_{t-1}^{(m)}, \mathbf{u}_t^{(m)}, \boldsymbol{\theta}^{(m)} \right), \quad t = 1, \dots, N, \quad m = 1, \dots, M \quad (3)$$

However, deterministic models do not inherently quantify uncertainty, which is critical for understanding the variability in soil responses and ensuring confidence in predictions. In contrast, probabilistic models explicitly quantify uncertainty, enabling richer representations of confidence in predictions.

To address this, a probabilistic mapping f_β that relates the previous state to the current state, conditioned on exogenous inputs and triaxial test constants, is proposed. Specifically, given M datasets, each structured as:

$$\mathcal{S}^{(m)} = \left\{ \mathbf{u}_{1:N}^{(m)}, \mathbf{s}_{1:N}^{(m)}, \boldsymbol{\theta}^{(m)} \right\}, \quad m = 1, \dots, M \quad (4)$$

The objective is to characterize the predictive probability distribution over the states \mathbf{s} , conditioned on the inputs \mathbf{u} and the test constants $\boldsymbol{\theta}$, expressed as:

$$p(\mathbf{s}_{1:N} \mid \mathbf{u}_{1:N}, \boldsymbol{\theta})$$

which encodes both the predictions and the associated uncertainties.

To facilitate efficient inference, the conditional distribution is modeled as a Gaussian distribution. The modeling choice simplifies the task by reducing it to the estimation of two key parameters: the mean and covariance of the Gaussian distribution. The proposed framework uses a generalized variational Bayesian inference integrated with a windowed recursive FFNN structure, to fit the probabilistic representation, quantifying uncertainty across load steps.

3 Methodology

The proposed framework combines the strengths of deterministic recursive FFNN models with the uncertainty quantification capabilities of Bayesian neural networks. A sliding-windowed recursive structure and pseudo-likelihood formulation address challenges specific to sequential triaxial test data, while variational inference enables tractable posterior estimation in high-dimensional parameter spaces. We first introduce rFFNNs and the sliding-window strategy, then extend them into recursive Bayesian FFNNs (rBNNs), which quantify both aleatoric and epistemic uncertainty. Finally, we outline the generalized likelihood, posterior approximation, and normalization used for model training.

3.1 Recursive Feedforward Neural Networks (rFFNNs)

Unlike standard FFNNs, which map one state to the next, rFFNNs recursively feed predictions back as inputs, reducing error accumulation over multi-step forecasts (Fig. 1b). This recursive loop allows rFFNNs to capture temporal dependencies and is well-suited to sequential constitutive modeling.

3.1.1 Sliding window approach for training rFFNNs

The loading series is divided into overlapping subsets or *sliding windows* of length H , each containing states, exogenous inputs, and test constants:

$$\mathcal{S}_{H,k}^{(m)} = \left\{ \mathbf{s}_{t-1}^{(m)}, \mathbf{u}_t^{(m)}, \boldsymbol{\theta}^{(m)} \right\}_{t=k}^{k+H-1}, \quad k = 1, \dots, N - H + 1, \quad m = 1, \dots, M \quad (5)$$

Here, $\mathcal{S}_{H,k}^{(m)}$ is a window from the m^{th} triaxial test, comprising triaxial test constants $\boldsymbol{\theta}$ and a certain H -long sequence of state variables \mathbf{s} and exogenous inputs \mathbf{u} . Training on windows (Fig. 3) localizes learning of temporal patterns. $H = 1$ reduces to a standard FFNN, while $H = N$ recovers a full-series rFFNN [21]. This flexibility allows the framework to balance the trade-off between capturing short-term patterns and long-term dependencies.

3.1.2 Recursive prediction within windowed subsets

For each window $\mathcal{S}_{H,k}^{(m)}$, the rFFNN performs recursive predictions starting with the initial measured state $\mathbf{s}_{k-1}^{(m)}$ to predict the next state $\hat{\mathbf{s}}_k^{(m)}$, given the input $\mathbf{u}_k^{(m)}$ and triaxial test constant $\boldsymbol{\theta}^{(m)}$. The predicted states are recursively fed back into the rFFNN, alongside the inputs from the subsequent load step, to predict the future states within the window. This recursive mechanism, illustrated in Fig. 4, can be expressed mathematically as:

$$\begin{aligned} \hat{\mathbf{s}}_k^{(m)} &= f_\beta \left(\mathbf{s}_{k-1}^{(m)}, \mathbf{u}_k^{(m)}, \boldsymbol{\theta}^{(m)} \right) \\ \hat{\mathbf{s}}_{k+1}^{(m)} &= f_\beta \left(\hat{\mathbf{s}}_k^{(m)}, \mathbf{u}_{k+1}^{(m)}, \boldsymbol{\theta}^{(m)} \right) \\ &\vdots \\ \hat{\mathbf{s}}_{k+H-1}^{(m)} &= f_\beta \left(\hat{\mathbf{s}}_{k+H-2}^{(m)}, \mathbf{u}_{k+H-1}^{(m)}, \boldsymbol{\theta}^{(m)} \right) \end{aligned} \quad (6)$$

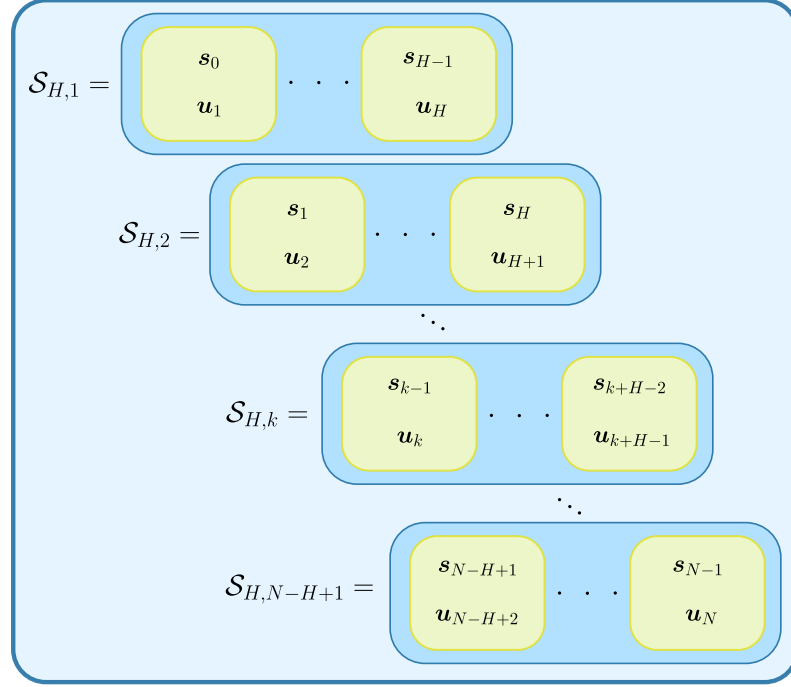


Figure 3: Sliding window segmentation of a triaxial loading sequence into overlapping subsequences of length H for rFFNN training.

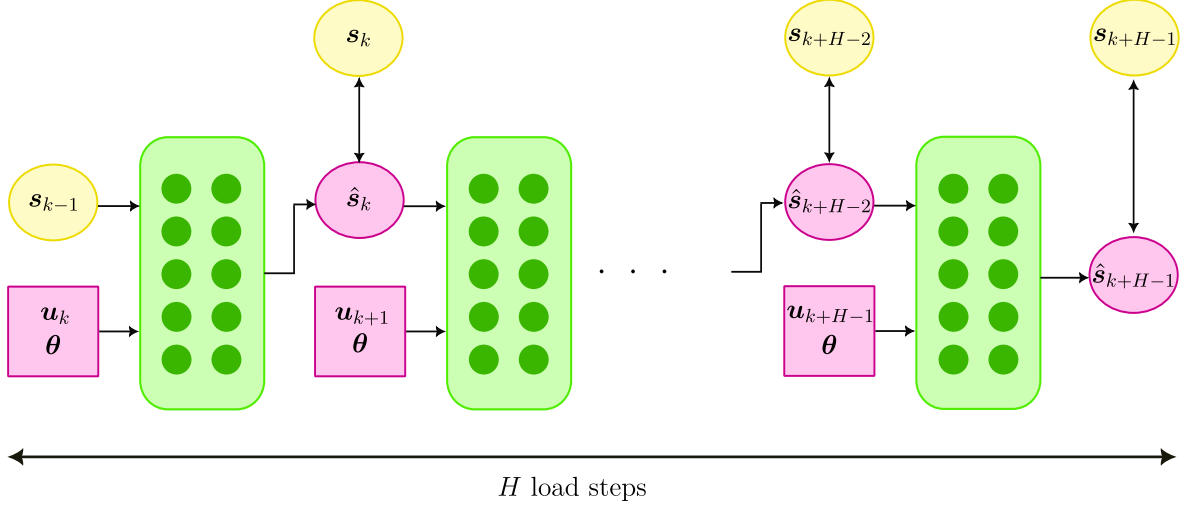


Figure 4: **Recursive state prediction over a H -length sliding window** using a deterministic rFFNN for the data subset $\mathcal{S}_{H,k}$.

3.1.3 Loss computation for training rFFNNs

The loss $L_{H,k}^{(m)}$ for a windowed subset $\mathcal{S}_{H,k}^{(m)}$ is computed as the average discrepancy between the predicted states $\hat{s}_t^{(m)}$ and the corresponding observed states $s_t^{(m)}$ across all load steps within the window, calculated as below:

$$L_{H,k}^{(m)} = \frac{1}{H} \sum_{t=k}^{k+H-1} \ell(s_t^{(m)}, \hat{s}_t^{(m)}) \quad (7)$$

The function ℓ is a user-chosen loss metric, such as the squared loss, absolute loss, and Huber loss, depending on the requirements of the application.

The average loss L across all loading series of states $\{s_{0:N}^{(m)}\}_{m=1}^M$, comprising M triaxial tests with N load steps each, is determined by summing the loss over all windowed subsets, given the complete loading series of control inputs $\{\mathbf{u}_{1:N}^{(m)}, \boldsymbol{\theta}^{(m)}\}_{m=1}^M$:

$$L = \sum_{m=1}^M \frac{1}{M(N-H+1)} \sum_{k=1}^{(N-H+1)} L_{H,k}^{(m)} \quad (8)$$

3.2 Generalized Bayesian rFFNNs (rBNNs)

Building upon the deterministic foundation of rFFNN, the next step involves integrating uncertainty quantification through Bayesian methods. The rBNN framework extends rFFNN by treating model parameters as random variables, allowing for probabilistic predictions and a richer representation of model uncertainty. This approach aligns closely with Bayesian neural networks (BNNs)[46, 52], which enables the estimation of both epistemic uncertainty (arising from limited training data) and aleatoric uncertainty (due to inherent noise in data). The key enhancement of rBNNs over rFFNNs is as follows:

- (a) *Random variable modeling*: The parameters of the rBNN, represented as the vector $\boldsymbol{\beta}$, are treated as a vector-valued random variable, characterized by a joint probability distribution. This allows the model to capture epistemic uncertainty.
- (b) *Deterministic output uncertainty layer*: A deterministic layer at the output of the rBNN predicts the mean and covariance of a Gaussian distribution for the next state, capturing aleatoric uncertainty due to noise in the training data.
- (c) *Use of pseudo-likelihood*: Unlike traditional Bayesian methods, where the likelihood is derived from a probabilistic model of the data, we employ a pseudo-likelihood derived from the recursive predictions over several overlapping subsets of data.

Illustration of the rBNN can be found in Fig. 5. In this formulation, the neural network parameters $\boldsymbol{\beta}$ are not directly learned, instead the posterior distribution over the parameter vector $\boldsymbol{\beta}$ is inferred within a *generalized* Bayesian framework.

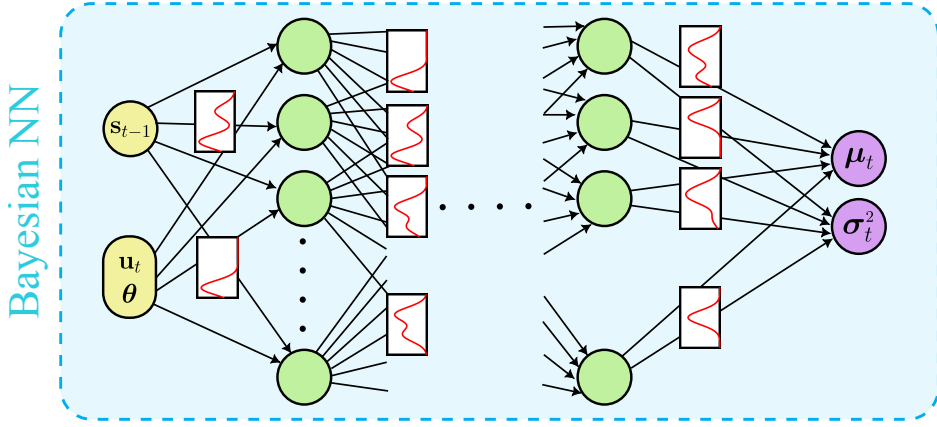


Figure 5: **Depiction of rBNN** where model parameters are treated as random variables, and the output layer predicts the mean and diagonal variances of a Gaussian distribution for the subsequent state.

However, the high dimensionality of parameter vector $\boldsymbol{\beta}$ makes posterior inference challenging: analytical solutions are intractable and Markov chain Monte Carlo (MCMC), though exact, is computationally prohibitive. Instead, we adopt variational Bayesian inference, which approximates the posterior with a simpler tractable family. The following

subsections present the key components of the generalized Bayesian rFFNN: prior, pseudo-likelihood, posterior approximation, and posterior predictive distribution.

3.2.1 Prior distribution

The prior distribution encodes initial beliefs about parameters β before observing data. A common choice in neural networks is a fully factorized standard Gaussian [54], where each $\beta_l \sim \mathcal{N}(0, 1)$, due to its simplicity and computational efficiency. Formally,

$$p(\beta) = \prod_{l=1}^L p(\beta_l) = \prod_{l=1}^L \mathcal{N}(\beta_l; 0, 1) = \mathcal{N}(\beta; \mathbf{0}, \mathbf{I}_L), \quad (9)$$

where L denotes the dimensionality of the model parameter vector β and \mathbf{I}_L represents the $L \times L$ identity matrix. This prior simplifies posterior inference, regularizes the model by favoring parameters near zero, and helps prevent overfitting in high-dimensional settings.

3.2.2 Pseudo-likelihood formulation

In classical Bayesian inference, the likelihood is derived from a probabilistic model of the data-generating process. For rFFNNs, however, the sliding-window approach reuses overlapping sequences, complicating a conventional likelihood. To address this, we employ a pseudo-likelihood, which acts like a loss function and efficiently handles overlapping data while enabling uncertainty quantification [55].

For the t^{th} load step in the k^{th} window of the m^{th} triaxial test, the conditional distribution of the state vector $\mathbf{s}_t^{(m)}$ is modeled as:

$$p(\mathbf{s}_t^{(m)} | \mathbf{s}_{t-1}^{(m)}, \mathbf{u}_t^{(m)}, \theta^{(m)}, \beta) = \mathcal{N}(\mathbf{s}_t^{(m)}; \boldsymbol{\mu}_t^{(m)}, \boldsymbol{\sigma}_t^{2(m)}) \quad (10)$$

where the predicted mean vector $\boldsymbol{\mu}_t^{(m)}$ and the predicted diagonal variance vector $\boldsymbol{\sigma}_t^{2(m)}$ are the two outputs of the neural network f_β :

$$\begin{aligned} \boldsymbol{\mu}_t^{(m)}(\beta) &= f_\beta(\mathbf{s}_{t-1}^{(m)}, \mathbf{u}_t^{(m)}, \theta^{(m)}) \\ \boldsymbol{\sigma}_t^{2(m)}(\beta) &= f_\beta(\mathbf{s}_{t-1}^{(m)}, \mathbf{u}_t^{(m)}, \theta^{(m)}) \end{aligned} \quad (11)$$

with β representing the neural network parameters (weights and biases).

We construct the likelihood for a H -length sliding window $\mathcal{S}_{H,k}^{(m)}$ by defining a joint distribution over the state sequence $\mathbf{s}_{k:k+H-1}^{(m)} = \{\mathbf{s}_k^{(m)}, \dots, \mathbf{s}_{k+H-1}^{(m)}\}$ for a given triaxial test m , with known initial state $\mathbf{s}_{k-1}^{(m)}$, as a product of conditional distributions:

$$\mathcal{L}_{H,k}^{(m)}(\beta) = p(\mathbf{s}_{k:k+H-1}^{(m)} | \mathbf{u}_{k:k+H-1}^{(m)}, \theta^{(m)}, \beta) = \prod_{t=k}^{k+H-1} p(\mathbf{s}_t^{(m)} | \mathbf{s}_{t-1}^{(m)}, \mathbf{u}_t^{(m)}, \theta^{(m)}, \beta) \quad (12)$$

However, propagating the full joint distribution across the load steps is computationally prohibitive, especially for overlapping windows across multiple triaxial tests. To simplify, we approximate the joint likelihood using a pseudo-likelihood formulation, where the state at load t depends on the predicted mean of the previous state rather than its sampled value:

$$\begin{aligned} \mathcal{L}_{H,k}^{(m)}(\beta) &= p(\mathbf{s}_k^{(m)} | \mathbf{s}_{k-1}^{(m)}, \mathbf{u}_k^{(m)}, \theta^{(m)}, \beta) \prod_{t=k+1}^{k+H-1} p(\mathbf{s}_t^{(m)} | \boldsymbol{\mu}_{t-1}^{(m)}, \mathbf{u}_t^{(m)}, \theta^{(m)}, \beta) \\ &= \mathcal{N}(\mathbf{s}_k^{(m)}; \boldsymbol{\mu}_k^{(m)}(\beta), \boldsymbol{\sigma}_k^{2(m)}(\beta)) \prod_{t=k+1}^{k+H-1} \mathcal{N}(\mathbf{s}_t^{(m)}; \boldsymbol{\mu}_t^{(m)}(\beta), \boldsymbol{\sigma}_t^{2(m)}(\beta)) \end{aligned} \quad (13)$$

This approximation reduces computational complexity and memory usage while maintaining key uncertainty quantification features.

Substituting the expression of the Gaussian distribution into the pseudo-likelihood and ignoring terms that are constant with respect to the network parameters β , the log-joint-pseudo-likelihood for the k^{th} window becomes:

$$\log \mathcal{L}_{H,k}^{(m)}(\beta) = -\frac{1}{2} \sum_{t=k}^{k+H-1} \left(\log \det(\text{diag}(\boldsymbol{\sigma}_t^{2(m)})) + (\mathbf{s}_t^{(m)} - \boldsymbol{\mu}_t^{(m)})^T \{\text{diag}(\boldsymbol{\sigma}_t^{2(m)})\}^{-1} (\mathbf{s}_t^{(m)} - \boldsymbol{\mu}_t^{(m)}) \right) \quad (14)$$

The average log-pseudo-likelihood for the entire sequential loading of states $\mathcal{D} = \{s_{0:N}^{(m)}\}_{m=1}^M$, consisting of M triaxial tests, each with N load steps, given entire sequential loading series of control inputs $\mathcal{U} = \{u_{1:N}^{(m)}, \theta^{(m)}\}_{m=1}^M$ is computed by summing the log-pseudo-likelihoods over all windowed subsets:

$$\log \mathcal{L}(\beta) = \log p(\mathcal{D} | \beta, \mathcal{U}) = \sum_{m=1}^M \frac{1}{M(N-H+1)} \sum_{k=1}^{(N-H+1)} \log \mathcal{L}_{H,k}^{(m)}(\beta) \quad (15)$$

where $N - H + 1$ is the total number of sliding windows per triaxial test.

3.2.3 Parameter posterior approximation via generalized variational inference

In Bayesian inference, the parameter posterior distribution $p(\beta | \mathcal{D}, \mathcal{U})$ encapsulates our updated beliefs about the parameters β after observing the data \mathcal{D} . However, in practice, directly computing the posterior is computationally intractable for high-dimensional parameter spaces, such as those encountered in neural networks. This intractability arises due to the complexity of marginalizing over the parameter space to compute the evidence $p(\mathcal{D} | \mathcal{U})$. To address this issue, we employ variational inference (VI) that provides a scalable framework for approximating the posterior distribution through optimization.

Variational formulation Variational inference introduces a family of tractable distributions $q_\eta(\beta)$ parameterized by η , which is designed to approximate the true posterior $p(\beta | \mathcal{D}, \mathcal{U})$. The goal is to find the member of the variational family $q_\eta(\beta)$ that minimizes the Kullback-Leibler (KL) divergence – which measures the information lost in approximation – to the true posterior:

$$D_{\text{KL}}(q_\eta(\beta) \| p(\beta | \mathcal{D}, \mathcal{U})) = \mathbb{E}_{q_\eta(\beta)} [\log q_\eta(\beta) - \log p(\beta | \mathcal{D}, \mathcal{U})] \quad (16)$$

Direct minimization of D_{KL} is not feasible because the true posterior $p(\beta | \mathcal{D}, \mathcal{U})$ involves the intractable evidence $p(\mathcal{D})$. Instead, VI maximizes a surrogate objective called the *Evidence Lower Bound* (ELBO), which is derived from the decomposition of the log evidence, as follows:

$$\log p(\mathcal{D} | \mathcal{U}) = \mathbb{E}_{q_\eta(\beta)} \left[\log \frac{p(\mathcal{D}, \beta | \mathcal{U})}{q_\eta(\beta)} \right] + D_{\text{KL}}(q_\eta(\beta) \| p(\beta | \mathcal{D}, \mathcal{U})) \quad (17)$$

where the second term is the KL divergence, which is always non-negative. This implies:

$$\log p(\mathcal{D} | \mathcal{U}) \geq \mathbb{E}_{q_\eta(\beta)} \left[\log \frac{p(\mathcal{D}, \beta | \mathcal{U})}{q_\eta(\beta)} \right] \triangleq \mathcal{L}_{\text{ELBO}} \quad (18)$$

The ELBO can be further decomposed into two terms:

$$\mathcal{L}_{\text{ELBO}} = \mathbb{E}_{q_\eta(\beta)} [\log p(\mathcal{D} | \mathcal{U}, \beta)] - D_{\text{KL}}(q_\eta(\beta) \| p(\beta)) \quad (19)$$

where the first term is the expected log-likelihood and it measures how well the variational distribution $q_\eta(\beta)$ fits the observed data, and the second term is the KL divergence from prior that regularizes the variational distribution $q_\eta(\beta)$ by penalizing it from deviating too far from the prior $p(\beta)$. It can be observed that maximizing the ELBO is equivalent to minimizing the KL divergence (the second term).

Monte Carlo approximation of ELBO The expectation in the computation of ELBO is approximated using Monte Carlo integration by drawing i.i.d. samples from the variational distribution $q_\eta(\beta)$:

$$\mathbb{E}_{q_\eta(\beta)} [\log p(\mathcal{D} | \beta, \mathcal{U})] \approx \frac{1}{N_q} \sum_{i=1}^{N_q} \log p(\mathcal{D} | \beta^{(i)}, \mathcal{U}), \quad \beta^{(i)} \sim q_\eta(\beta) \quad (20)$$

where N_q is the number of Monte Carlo samples (set to $N_q = 25$ in this study although even one sample suffices accordingly to [56]).

The prior regularization term, $D_{\text{KL}}(q_\eta(\beta) \| p(\beta))$, is computed analytically, especially when the variational distribution $q_\eta(\beta)$ and prior $p(\beta)$ are both Gaussian.

Choice of variational distribution To make the optimization tractable, the variational distribution $q_\eta(\beta)$ is typically chosen to belong to a parameterized class of distributions. A common choice is the fully-factorized Gaussian distribution:

$$q_\eta(\beta) = \prod_{i=1}^L \mathcal{N}(\beta_i; \mu_i^q, (\sigma_i^q)^2) \quad (21)$$

where $\eta = \{\mu^q, \sigma^q\}$, with μ^q and σ^q representing the mean vector and diagonal covariance matrix of the variational posterior.

Optimization of variational parameters The variational parameters $\boldsymbol{\eta}$ are optimized by maximizing the ELBO using gradient-based optimization. The reparameterization trick [57] is often employed to backpropagate through the sampling process:

$$\boldsymbol{\beta} = \boldsymbol{\mu}^q + \log(1 + \exp(\boldsymbol{\sigma}^q)) \odot \boldsymbol{\gamma} \quad (22)$$

where $\boldsymbol{\gamma}$ is a noise variable independent of $\boldsymbol{\mu}$ and $\boldsymbol{\Sigma}$, sampled from a standard Gaussian distribution $\mathcal{N}(\boldsymbol{\gamma}; \mathbf{0}, \mathbf{I}_L)$ and \odot represents elementwise multiplication. This parameterization expresses $\boldsymbol{\beta}$ as a deterministic function of $\boldsymbol{\mu}^q$, $\boldsymbol{\sigma}^q$ and the random variable $\boldsymbol{\gamma}^q$, allowing flow of gradients via backpropagation through the parameters $\boldsymbol{\mu}$ and $\boldsymbol{\Sigma}$ during optimization. Note the use of softplus function $\log(1 + \exp(\cdot))$ is to ensure the positivity of standard deviation $\boldsymbol{\sigma}^q$ during optimization. However, it is common to minimize a function than maximize, hence the ELBO maximization is turned into a minimization problem by minimizing the negative of ELBO. Hence the optimization problem to be solved is that of minimization of the negative of ELBO with respect to the variational parameters:

$$\begin{aligned} \boldsymbol{\mu}_*^q, \boldsymbol{\sigma}_*^q &= \arg \min -\mathcal{L}_{\text{ELBO}} \\ &= \arg \min -\mathbb{E}_{q_\eta(\boldsymbol{\beta})} [\log p(\mathcal{D} | \boldsymbol{\beta}, \mathcal{U})] + D_{\text{KL}}(q_\eta(\boldsymbol{\beta}) \| p(\boldsymbol{\beta})) \\ &\approx \arg \min -\frac{1}{N_q} \sum_{i=1}^{N_q} \log p(\mathcal{D} | \boldsymbol{\beta}^{(i)}) + D_{\text{KL}}(q_\eta(\boldsymbol{\beta}^{(i)}) \| p(\boldsymbol{\beta}^{(i)})) \\ &= -\frac{1}{N_q} \sum_{i=1}^{N_q} \log p(\mathcal{D} | \boldsymbol{\beta}^{(i)}) + \sum_{i=1}^L \left[-\log \sigma_i^q + \frac{1}{2} ((\mu_i^q)^2 + (\sigma_i^q)^2 - 1) \right] \end{aligned} \quad (23)$$

where $\boldsymbol{\beta}^{(i)} \sim q_\eta(\boldsymbol{\beta})$. The gradients required to optimize the variational parameters $\boldsymbol{\eta} = [\boldsymbol{\mu}^q, \boldsymbol{\sigma}^q]$ are computed using the Bayes-by-Backprop [58]:

$$\Delta \boldsymbol{\mu}^q = -\left(\frac{\partial \mathcal{L}_{\text{ELBO}}}{\partial \boldsymbol{\beta}} + \frac{\partial \mathcal{L}_{\text{ELBO}}}{\partial \boldsymbol{\mu}^q} \right) \quad (24a)$$

$$\Delta \boldsymbol{\sigma}^q = -\left(\frac{\partial \mathcal{L}_{\text{ELBO}}}{\partial \boldsymbol{\beta}} \frac{\boldsymbol{\epsilon}}{1 + \exp(-\boldsymbol{\sigma}^q)} + \frac{\partial \mathcal{L}_{\text{ELBO}}}{\partial \boldsymbol{\sigma}^q} \right) \quad (24b)$$

where the term $\frac{\partial \mathcal{L}_{\text{ELBO}}}{\partial \boldsymbol{\beta}}$ is computed via standard backpropagation. The overall training procedure is outlined in Algorithm 1. Once training is complete, the proposed rBNN model is used recursively to predict across H steps, requiring only the state parameters at $t = 0$ and exogenous inputs.

Connection to generalized variational inference In this work, the expected log-likelihood term in the ELBO (refer Eq. (19)) is approximated using the pseudo-likelihood formulation described in Section 3.2.2. This formulation aligns with generalized variational inference (GVI) as outlined in [59]. GVI extends the classical Bayesian framework to accommodate cases where the likelihood function is replaced by a loss-like function (or a generalized risk function). This departure from strict likelihood-based inference allows for greater flexibility in handling cases where the likelihood is replaced with a pseudo-likelihood for task-specific objectives. Using generalized variational inference enables efficient computation of the variational objective while incorporating the overlapping structure of the data introduced by the sliding window approach.

3.3 Posterior prediction

Once the optimized variational distribution $q_{\boldsymbol{\eta}_*}(\boldsymbol{\beta})$ is obtained, the trained rBNN model can predict the complete stress-strain-volume change curve for previously unseen test scenarios. This prediction is conditioned on the initial state parameters \mathbf{s}_0^* at $t = 0$ and the sequence of exogenous inputs $\{\mathbf{u}_{1:N_*}^*, \boldsymbol{\theta}^*\}$, where N_* represents the number of prediction load steps. The predictive probability of the states $\{\mathbf{s}_{1:N_*}^*\}$ is obtained by marginalizing over the posterior weights:

$$p(\mathbf{s}_{1:N_*}^* | \mathbf{u}_{1:N_*}^*, \mathbf{s}_0^*, \boldsymbol{\theta}^*, \mathcal{D}, \mathcal{U}) = \int p(\mathbf{s}_{1:N_*}^* | \mathbf{u}_{1:N_*}^*, \mathbf{s}_0^*, \boldsymbol{\theta}^*, \boldsymbol{\beta}) p(\boldsymbol{\beta} | \mathcal{D}, \mathcal{U}) d\boldsymbol{\beta} \quad (25)$$

To make this computationally feasible, the posterior $p(\boldsymbol{\beta} | \mathcal{D}, \mathcal{U})$ is approximated using the optimized variational distribution $q_{\boldsymbol{\eta}_*}(\boldsymbol{\beta})$. The predictive distribution is then approximated via Monte Carlo sampling:

$$\begin{aligned} p(\mathbf{s}_{1:N_*}^* | \mathbf{u}_{1:N_*}^*, \mathbf{s}_0^*, \boldsymbol{\theta}^*, \mathcal{D}, \mathcal{U}) &= \int p(\mathbf{s}_{1:N_*}^* | \mathbf{u}_{1:N_*}^*, \mathbf{s}_0^*, \boldsymbol{\theta}^*, \boldsymbol{\beta}) q_{\boldsymbol{\eta}_*}(\boldsymbol{\beta}) d\boldsymbol{\beta} \\ &\approx \frac{1}{N_{\text{mc}}} \sum_{i=1}^{N_{\text{mc}}} p(\mathbf{s}_{1:N_*}^* | \mathbf{u}_{1:N_*}^*, \mathbf{s}_0^*, \boldsymbol{\theta}^*, \boldsymbol{\beta}^{(i)}), \quad \boldsymbol{\beta}^{(i)} \sim q(\boldsymbol{\beta}; \boldsymbol{\eta}_*) \end{aligned} \quad (26)$$

where, $N_{mc} = 1000$ denotes the number of Monte Carlo samples. The choice of 1000 samples was guided by empirical experiments, ensuring stable estimates of the predictive mean and variance without incurring excessive computational costs.

Given the Gaussian likelihood structure of the predictive model and the Gaussian variational distribution, the predictive distribution becomes Gaussian:

$$\begin{aligned} p(s_{1:N_*}^* | \mathbf{u}_{1:N_*}^*, s_0^*, \boldsymbol{\theta}^*, \mathcal{D}, \mathcal{U}) &\approx \frac{1}{N_{mc}} \sum_{i=1}^{N_{mc}} \mathcal{N}(s_{1:N_*}^* | \mathbf{u}_{1:N_*}^*, s_0^*, \boldsymbol{\theta}^*, \boldsymbol{\beta}^{(i)}), \quad \boldsymbol{\beta}^{(i)} \sim \mathcal{N}(\boldsymbol{\beta}; \boldsymbol{\mu}_\star^q, (\sigma_\star^q)^2) \\ &= \frac{1}{N_{mc}} \sum_{i=1}^{N_{mc}} \prod_{j=1}^{N_*} \mathcal{N}(s_j^* | \boldsymbol{\mu}_j^* (\boldsymbol{\beta}^{(i)}), (\sigma_j^*)^2 (\boldsymbol{\beta}^{(i)})) \end{aligned} \quad (27)$$

where $\boldsymbol{\mu}_j^*$ and $(\sigma_j^*)^2$ are the mean and variance of the states at load step j , respectively. The recursive nature of the model allows the joint likelihood to be factorized as a product of individual conditional distributions, akin to Eq. (12).

Since the predictive distribution over the states is a Gaussian distribution, it is sufficient to compute the predictive mean and variance vectors directly through Monte Carlo sampling:

$$\boldsymbol{\mu}_j^* = \frac{1}{N_{mc}} \sum_{i=1}^{N_{mc}} \boldsymbol{\mu}_j(s_{j-1}^*, \boldsymbol{\theta}^*, \mathbf{u}_j^*, \boldsymbol{\beta}^{(i)}), \quad \boldsymbol{\beta}^{(i)} \sim \mathcal{N}(\boldsymbol{\beta}; \boldsymbol{\mu}_\star^q, (\sigma_\star^q)^2) \quad (28a)$$

$$(\sigma_j^*)^2 = \frac{1}{N_{mc}} \sum_{i=1}^{N_{mc}} \sigma_j^2(s_{j-1}^*, \boldsymbol{\theta}^*, \mathbf{u}_j^*, \boldsymbol{\beta}^{(i)}), \quad \boldsymbol{\beta}^{(i)} \sim \mathcal{N}(\boldsymbol{\beta}; \boldsymbol{\mu}_\star^q, (\sigma_\star^q)^2) \quad (28b)$$

The mean and diagonal variance vectors can then be used to construct confidence intervals and quantify uncertainty. A small predictive posterior uncertainty in $\boldsymbol{\beta}$ leads to narrower confidence intervals, reflecting higher predictive certainty, and vice versa.

3.4 Data normalization

Scaling input data is essential in deep learning to avoid ill-conditioning and ensure stable convergence. For soil stress–strain modeling, this is particularly important since stress invariants p and q are strongly influenced by the initial confining pressure σ_3 , which governs yield strength and test evolution. Proper normalization is thus required to capture underlying physical trends.

To achieve this, the M triaxial tests are partitioned into J subsets, where each subset \mathcal{W}_j ($j = 1, \dots, J$) corresponds to a unique confining pressure. Within each subset, Root-Mean-Squared (RMS) values of p and q are computed across all tests and used as normalization factors:

$$\bar{p}_t^{(m)} = \frac{p_t^{(m)}}{p_{\mathcal{W}_j}^{(m)}}, \quad m \in \mathcal{W}_j, \quad p_{\text{rms}}^{\mathcal{W}_j} = \sqrt{\frac{1}{|\mathcal{W}_j| N} \sum_{m \in \mathcal{S}_j} \sum_{t=1}^N (p_t^{(m)})^2} \quad (29a)$$

$$\bar{q}_t^{(m)} = \frac{q_t^{(m)}}{q_{\mathcal{W}_j}^{(m)}}, \quad m \in \mathcal{W}_j, \quad q_{\text{rms}}^{\mathcal{W}_j} = \sqrt{\frac{1}{|\mathcal{W}_j| N} \sum_{s=1}^{S_j} \sum_{t=1}^N (q_t^{(s)})^2} \quad (29b)$$

Here N is the number of load steps, and $|\mathcal{W}_j|$ the number of tests in the subset. This subset-specific scheme was chosen over global normalization to retain variability linked to confining pressure, avoiding bias in model training.

Other variables—void ratio (e), exogenous inputs (\mathbf{u}), and triaxial test constants ($\boldsymbol{\theta}$)—are globally min–max scaled across all M tests:

$$\bar{x}_t^{(m)} = \frac{x_t^{(m)} - \min_{t,m} x_t^{(m)}}{\max_{t,m} x_t^{(m)} - \min_{t,m} x_t^{(m)}} \quad \text{for } x \in \{e, u_i\} \quad (30a)$$

$$\bar{\theta}_i(m) = \frac{\theta_i^{(m)} - \min_m \theta_i^{(m)}}{\max_m \theta_i^{(m)} - \min_m \theta_i^{(m)}} \quad (30b)$$

Algorithm 1 Training procedure for rBNN

Require: Training dataset $\mathcal{D} = \{\mathbf{s}_{0:N}^{(m)}\}_{m=1}^M$, $\mathcal{U} = \{\mathbf{u}_{1:N}^{(m)}, \boldsymbol{\theta}^{(m)}\}_{m=1}^M$, Sliding window length H

- 1: Data preprocessing
 - Normalize the stress invariants p and q using subset-based-RMS values (Eq. (29)), and e , \mathbf{u} , and $\boldsymbol{\theta}$ using min-max scaling (Eq. (30))
 - Using the normalized input data, create $M(N - H + 1)$ windowed subsets of data $\mathcal{S}_{H,k}^{(m)}$ according to Eq. (5)
- 2: Define model parameter prior: $\boldsymbol{\beta} \sim \mathcal{N}(\boldsymbol{\beta}; \mathbf{0}, \mathbf{I}_L)$
- 3: Initialize variational parameters $\boldsymbol{\mu}^q$ and $\boldsymbol{\sigma}^q$ (using random initialization)
- 4: **for** $\rho = 1$ to epochs: **do**
- 5: **for** $i = 1$ to N_q : **do**
 - Sample noise: $\boldsymbol{\gamma}^{(i)} \sim \mathcal{N}(\boldsymbol{\gamma}; \mathbf{0}, \mathbf{I}_L)$
 - Reparameterize weights: $\boldsymbol{\beta}^{(i)} = \boldsymbol{\mu}^q + \log(1 + \exp(\boldsymbol{\sigma}^q)) \odot \boldsymbol{\gamma}^{(i)}$
 - Perform a recursive forward pass by propagating inputs \mathcal{U} along with $\boldsymbol{\beta}^{(i)}$ to compute Eq. (11)
 - Compute the log-pseudo-likelihood using Eqs. (14) and (15)
- 6: **end for**
- 7: Given $\boldsymbol{\mu}^q$ and $\boldsymbol{\sigma}^q$, sample N_q i.i.d. samples of $\boldsymbol{\beta}$ from $q_{\eta}(\boldsymbol{\beta})$ distribution
- 8: Approximate the ELBO from Eq. (19) using N_q samples of $\boldsymbol{\beta}$
- 9: Compute the gradients of the negative ELBO w.r.t. variational parameters $\Delta\boldsymbol{\mu}_q$ and $\Delta\boldsymbol{\sigma}_q$ using Eq. (24)
- 10: Update the variational parameters using Adam optimizer with learning rate λ :

$$\boldsymbol{\mu}_q \leftarrow \boldsymbol{\mu}_q - \lambda \cdot \Delta\boldsymbol{\mu}_q$$

$$\boldsymbol{\sigma}_q \leftarrow \boldsymbol{\sigma}_q - \lambda \cdot \Delta\boldsymbol{\sigma}_q$$
- 11: **end for**
- 12: **Output:** Converged values of variational parameters $\boldsymbol{\eta}_{\star} = \{\boldsymbol{\mu}_{\star}^q, \boldsymbol{\sigma}_{\star}^q\}$

4 Performance assessment

This section evaluates deep learning models on monotonic and cyclic triaxial test data. For each loading condition, two datasets are used: numerically simulated tests for benchmarking and experimental tests on sand specimens for real-world validation. The workflow involves preprocessing, model training, and evaluation using standard error metrics. Finally, a comparative assessment of the results obtained from different deep-learning models is presented.

The monotonic datasets include 78 simulated (in Section 4.1.1) and 28 experimental CD tests (Section 4.2.1), while the cyclic datasets comprise 32 simulated (drained and undrained) (in Section 4.1.2) and 37 experimental CU tests (in Section 4.2.2). Each dataset was split into training, validation, and testing sets, with validation guiding hyperparameter selection.

Deterministic models (LSTM, GRU, Encoder–Decoder, rFFNN) were trained with the Huber loss (see Eq. (31)), balancing sensitivity to small and large residuals. The rBNN employed the negative ELBO loss, given by Eq. (19), combining posterior approximation with predictive accuracy.

$$\ell_{\text{Huber}}(x, \hat{x}) = \begin{cases} \frac{1}{2}(x - \hat{x})^2, & \text{if } |x - \hat{x}| < 1 \\ |x - \hat{x}| - \frac{1}{2}, & \text{otherwise} \end{cases} \quad (31)$$

Model performance on the validation and testing set (denoted by subscript $*$) was evaluated using two key error metrics: RMSE and MAE. These metrics were computed on the predicted states, which could either be scalar components (p_* , q_* , or e_*) or full vector-valued $\mathbf{s}_* = [p_*, q_*, e_*]$. With $\hat{\mathbf{s}}_{t*}^{(m)}$ and $\mathbf{s}_{t*}^{(m)}$ denoting the predicted and observed values, respectively, of the state variable at load-step t for the m^{th} experimental sample, the metrics are defined as follows:

$$\text{RMSE} = \frac{1}{M_* N_*} \sum_{m=1}^{M_*} \sum_{n=1}^{N_*} \left\| \mathbf{s}_{t*}^{(m)} - \hat{\mathbf{s}}_{t*}^{(m)} \right\|_2 \quad (32a)$$

$$\text{MAE} = \frac{1}{M_* N_*} \sum_{m=1}^{M_*} \sum_{n=1}^{N_*} \left\| \mathbf{s}_{t*}^{(m)} - \hat{\mathbf{s}}_{t*}^{(m)} \right\|_1 \quad (32b)$$

Here, M_* denotes the total number of triaxial tests in the evaluation (validation or test) set, and N_* denotes the number of load steps in the evaluation sets. In the case of scalar-valued predictions (e.g. p_* , q_* , e_*) the vector norms reduce to scalar operations.

A critical hyperparameter for both rFFNN and rBNN models is the window length (H), which determines the temporal context for training. H was chosen using the validation set.

4.1 Evaluation on simulated data

4.1.1 Monotonic Loading

Synthetic stress–strain–volume change data were generated through CD triaxial tests simulated in PLAXIS 3D using the hardening soil model [60]. Model parameters were chosen to reflect realistic sand behavior: the internal friction angle $\phi = 30^\circ$ for loose and 40° for dense sand, and the reference secant stiffness modulus $E_{50}^{\text{ref}} = 10\text{--}50 \text{ kPa}$ [61]. A constant dilatancy angle ψ of 5° was applied. A cohesion of 1 kPa ensured numerical stability. Representative stress–strain responses under varying confining pressures are shown in Fig. 6.

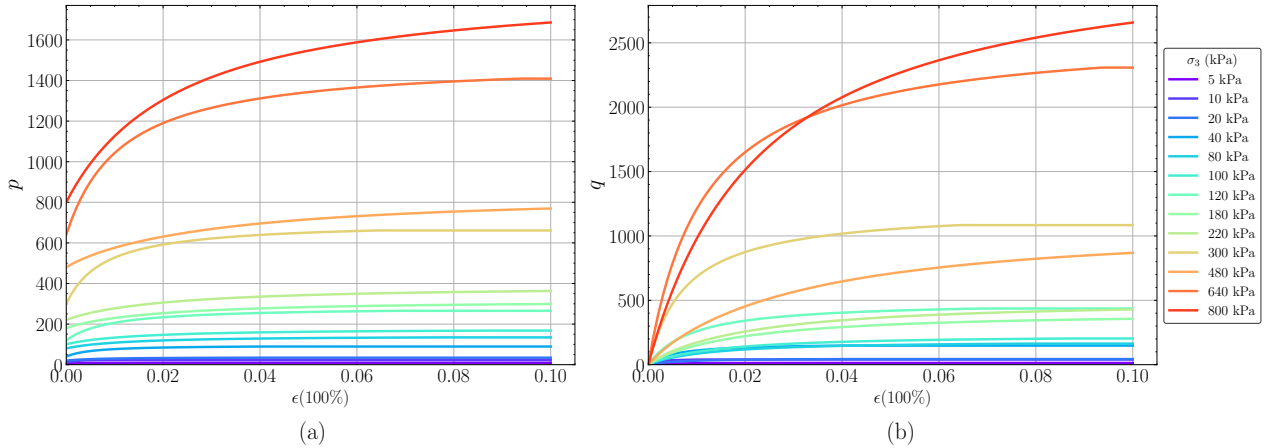


Figure 6: **Representative stress-strain curves** from simulated CD triaxial tests on sand specimens using the hardening soil model: (a) mean effective stress (p) versus axial strain (ϵ) in %; (b) deviatoric stress (q) versus axial strain (ϵ) in %, illustrating the response under varying confining pressures.

The dataset comprised 78 tests with $N = 100$ strain increments (10% axial strain) across confining pressures 5, 10, 20, 40, 80, 100, 120, 180, 220, 300, 480, 640, and 800 kPa, covering low to high regimes. Data were split into training (20–480 kPa), validation (10, 640 kPa), and testing (5, 800 kPa), enabling assessment of extrapolation performance under extreme low- and high-confining pressure scenarios.

For rFFNN and rBNN, window length H was tuned on the validation set. rFFNN performed best at $H = 10$, minimizing RMSE and MAE, while rBNN balanced RMSE and negative log-likelihood (NLL) at $H = 7$ (see Fig. 7). At $H = 1$, rFFNN reduces to a standard FFNN.

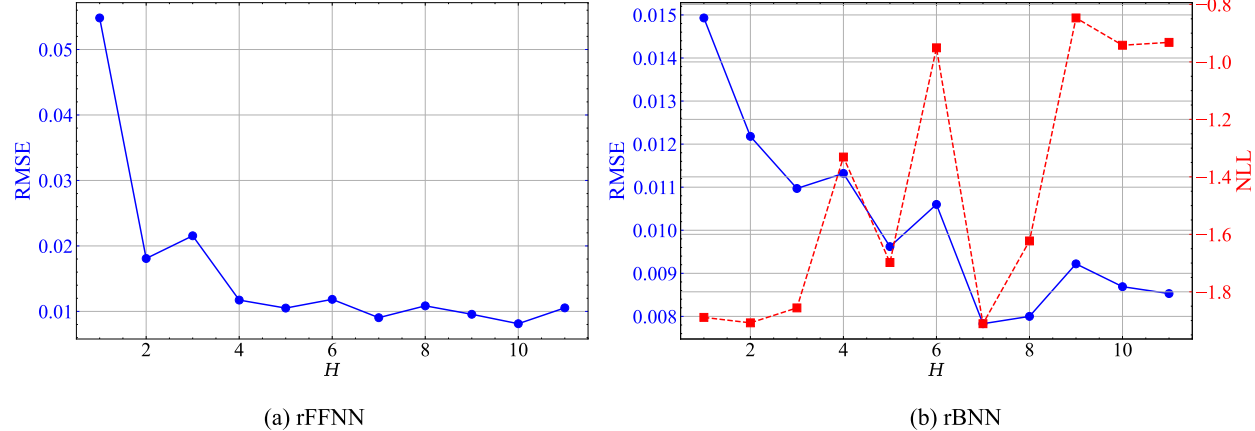


Figure 7: **Selection of H using the validation set of simulated case study:** (a) RMSE variation with window length H for rFFNN; (b) RMSE and NLL variation with H for rBNN.

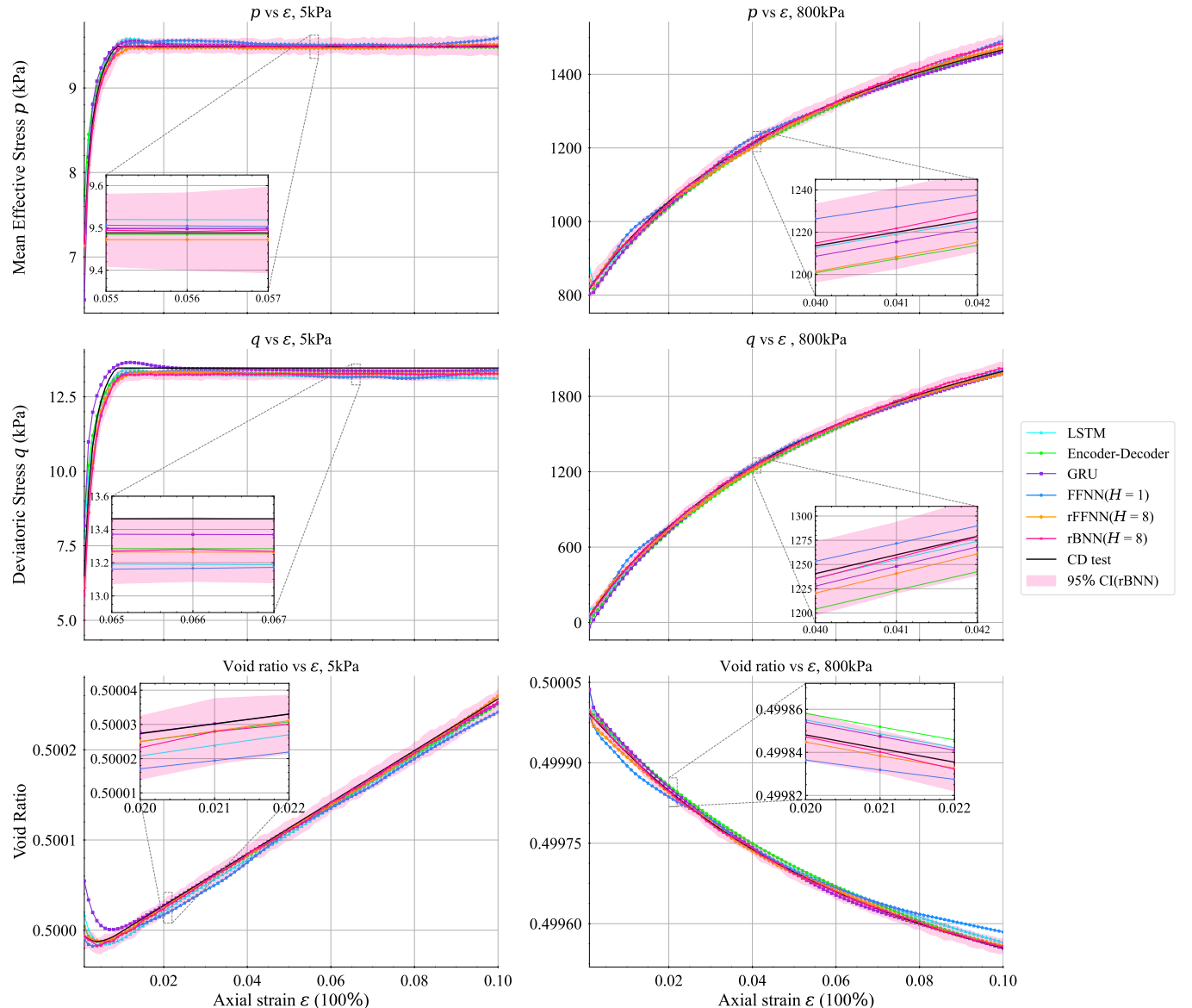


Figure 8: Comparison of model predictions for **mean effective stress p** , **deviatoric stress q** , and **void ratio** versus **axial strain ϵ** at two extreme confining pressures in simulated CD tests. Left column shows 5 kPa and right column shows 800 kPa results. Each subplot overlays predictions from various ML models, with the rBNN output including 95% confidence intervals.

The rBNN was trained with TensorFlow Probability [62] using the negative ELBO loss (Eq. (19)) for variational inference, with Monte Carlo sampling (see Section 3.3) to capture predictive uncertainty. Benchmark models (LSTM, GRU, Encoder–Decoder, FFNN, rFFNN) were trained with Huber loss, ReLU activations, and Adam optimizer [63], with an exponential learning rate scheduler to enhance training stability. Hyperparameters, including the number of layers, neurons per layer, and learning rates, were fine-tuned to minimize validation loss while ensuring stability. Architectures and configurations are listed in Table 1.

Table 1: **Architecture and training configurations** for models trained on simulated monotonic data.

Model	Hidden Layers	Neurons/Layer	Training Loss	Activation
LSTM($H=100$)	2	128	Huber	ReLU
Encoder-Decoder($H=100$)	2,2	128(per direction)	Huber	ReLU
GRU($H=100$)	2	128	Huber	ReLU
FFNN ($H=1$)	2	125	Huber	ReLU
rFFNN ($H=10$)	2	115	Huber	ReLU
rBNN ($H=7$)	3	100	– ELBO (Eq. (19))	ReLU

Performance on the test set is reported in Table 2. LSTM achieved the lowest MAE and RMSE across p , q , and e . rBNN and rFFNN followed closely, while Encoder–Decoder showed moderate performance, and GRU and FFNN the highest errors. Predictions under extreme pressures (5 and 800 kPa) are illustrated in Fig. 8.

Table 2: **Comparison of RMSE, and MAE on the test set** for DL models in the simulated monotonic dataset case, with bold values indicating the best performance for each parameter (p , q , e).

Models	p		q		e	
	MAE	RMSE	MAE	RMSE	MAE	RMSE
LSTM($H=100$)	0.0015	0.0020	0.0048	0.0060	0.0024	0.0030
Encoder-Decoder($H=100$)	0.0032	0.0065	0.0088	0.0109	0.0052	0.0081
GRU($H=100$)	0.0077	0.0098	0.0211	0.0252	0.0164	0.0202
FFNN($H=1$)	0.0058	0.0079	0.0152	0.0202	0.0132	0.0158
rFFNN($H=10$)	0.0032	0.0044	0.0109	0.0124	0.0046	0.0061
rBNN($H=7$)	0.0026	0.0039	0.0104	0.0125	0.0038	0.0054

Although LSTM gave the most accurate point predictions, rBNN provided uncertainty-aware forecasts with 95% confidence intervals encompassing the true responses, a key advantage for decision-making.

4.1.2 Cyclic Loading

To simulate the cyclic response of sandy soils, a synthetic dataset was generated using the exponential constitutive model [64], which captures stiffness degradation, strain accumulation, and phase transformation under drained and undrained triaxial conditions (see Eq. (33)):

$$\dot{\varepsilon}_v = M_{pt} |\dot{\varepsilon}_d| - \frac{q}{p'} \dot{\varepsilon}_d, \quad \dot{q} = 3G \left[\dot{\varepsilon}_d - \left(\frac{q}{p' M_p} \right) |\dot{\varepsilon}_d| \right] \quad (33)$$

Here \dot{q} is the deviatoric stress rate, $\dot{\varepsilon}_v$ the volumetric strain rate, and $\dot{\varepsilon}_d$ the deviatoric strain rate. In drained conditions, volumetric strain evolves freely. Under undrained loading, $\dot{\varepsilon}_v = 0$, producing pore pressure changes. Shear modulus G is nonlinear and stress-dependent, degrading with strain and void ratio. Strength parameters M_p and M_{pt} evolve with state variables, consistent with the critical state concept, and a nonlinear stress–dilatancy law simulates transitions between contractive and dilative responses. Model parameters follow [64] (Table 3).

Table 3: Constitutive model parameters adapted from [64]

G_0 (kPa)	ν	n	ϕ_c (°)	e_{c0}	λ	ξ	d
3000	0.3	0.67	31.2	0.937	0.022	0.71	2

Simulations included drained and undrained conditions, each with 16 strain-controlled cyclic triaxial tests. The initial void ratio e_0 was varied: 12 values for training (ranging from 0.625 to 0.925), one for validation (0.600), and three for

testing (0.575, 0.775, 0.950). Undrained tests used confining pressure of 300 kPa with axial strain amplitude ($-1\% - 1\%$); drained tests used 98 kPa. Each test produced a full cyclic stress–strain path.

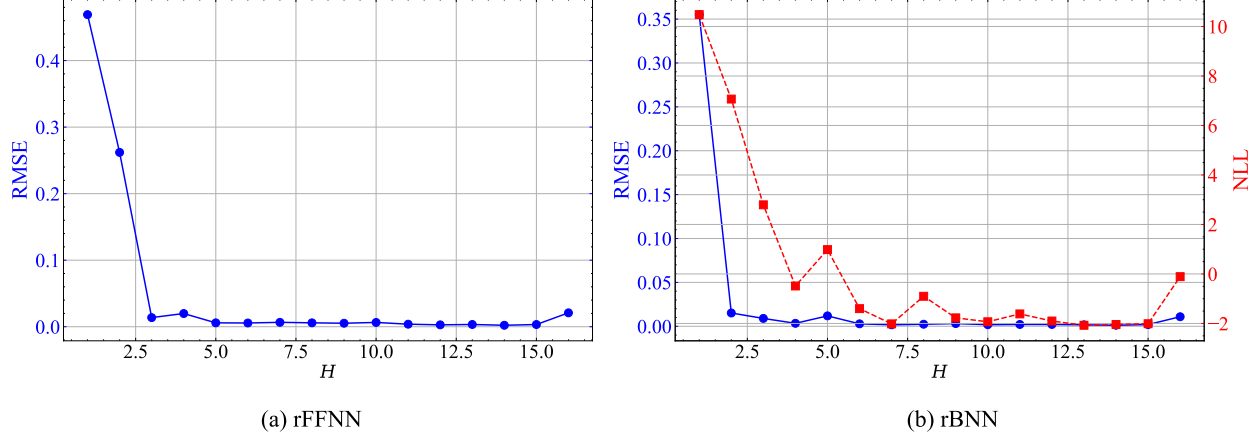


Figure 9: **Selection of H using the validation set of cyclic simulated case study:** (a) RMSE variation with window length H for rFFNN; (b) RMSE and NLL variation with H for rBNN.

The rFFNN and rBNN models were trained using the sliding window approach, with optimal window length $H = 14$ (see Fig. 9(a) and Fig. 9(b)). Deterministic baselines (LSTM, GRU, FFNN, and Encoder–Decoder) were optimized via validation (Table 4).

Table 4: **Architecture and training configurations** for models trained on simulated cyclic data.

Model	Hidden Layers	Neurons/Layer	Training Loss	Activation
LSTM($H=299$)	2	128	Huber	ReLU
Encoder-Decoder($H=299$)	2,2	128 (per direction)	Huber	ReLU
GRU($H=299$)	2	128	Huber	ReLU
FFNN($H=1$)	2	110	Huber	ReLU
rFFNN($H=14$)	2	110	Huber	ReLU
rBNN ($H=14$)	2	110	– ELBO (Eq. (19))	ReLU

Table 5: **Comparison of RMSE and MAE on the test set** for DL models in the simulated cyclic dataset case, with bold values indicating the best performance for each parameter (p, q, ϵ_v).

Models	p		q		ϵ_v	
	MAE	RMSE	MAE	RMSE	MAE	RMSE
LSTM($H=299$)	0.0561	0.1067	0.0248	0.0560	0.0054	0.0076
Encoder-Decoder($H=299$)	0.0613	0.1294	0.0301	0.0801	0.0069	0.0109
GRU($H=299$)	0.2101	0.4482	0.1188	0.2180	0.0866	0.1256
rFFNN($H=1$)	0.0406	0.0875	0.0283	0.0683	0.0057	0.0120
rFFNN($H=14$)	0.0286	0.0663	0.0215	0.0456	0.0081	0.0113
rBNN($H=14$)	0.0215	0.0469	0.0131	0.0355	0.0027	0.0042

Table 5 shows that rBNN achieved the lowest MAE and RMSE across p, q , and ϵ_v , followed by rFFNN. Recurrent models performed worse, particularly GRU. rBNN further provided well-calibrated uncertainty estimates. Figures 10 and 11 compare predictions under drained and undrained tests. The rBNN accurately reproduced cyclic stress–strain behavior, capturing contractive vs. dilative responses and stress degradation. Uncertainty bands encompassed true responses, demonstrating reliability in both interpolation (Figure 10(left)) and extrapolation (Figure 10(right)) scenarios. It correctly identifies the high liquefaction susceptibility of looser samples, confirming its reliability in modeling cyclic degradation and liquefaction phenomena.

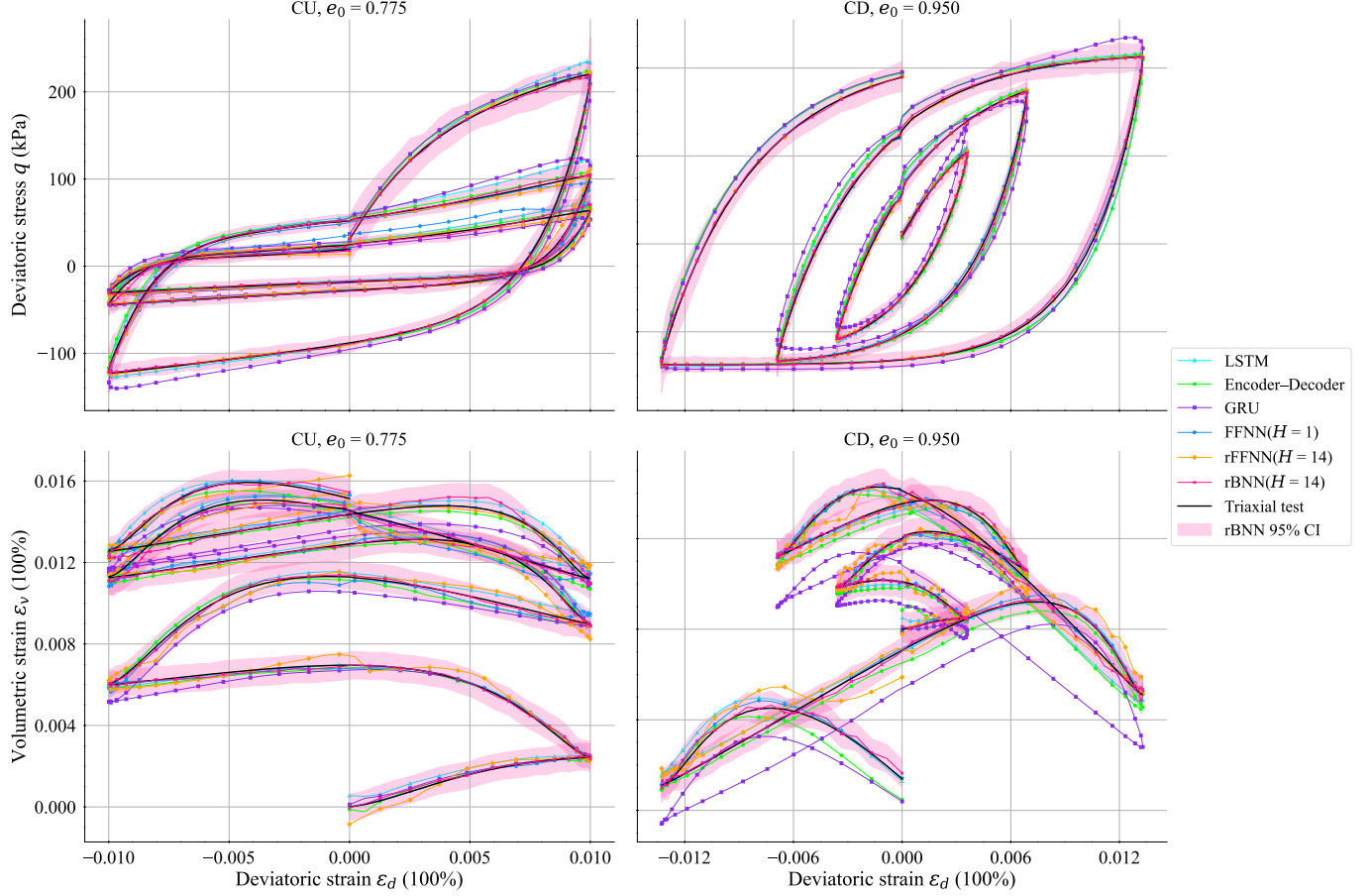


Figure 10: Comparison of model predictions on the test set for **deviatoric stress q** and **volumetric strain ε_v** versus **deviatoric strain ε_d** in simulated cyclic triaxial tests. Left column corresponds to an **undrained test** with initial void ratio $e_0 = 0.775$, and right column to a **drained test** with $e_0 = 0.950$. Each subplot overlays predictions from various ML models, with the rBNN output including 95% confidence intervals.

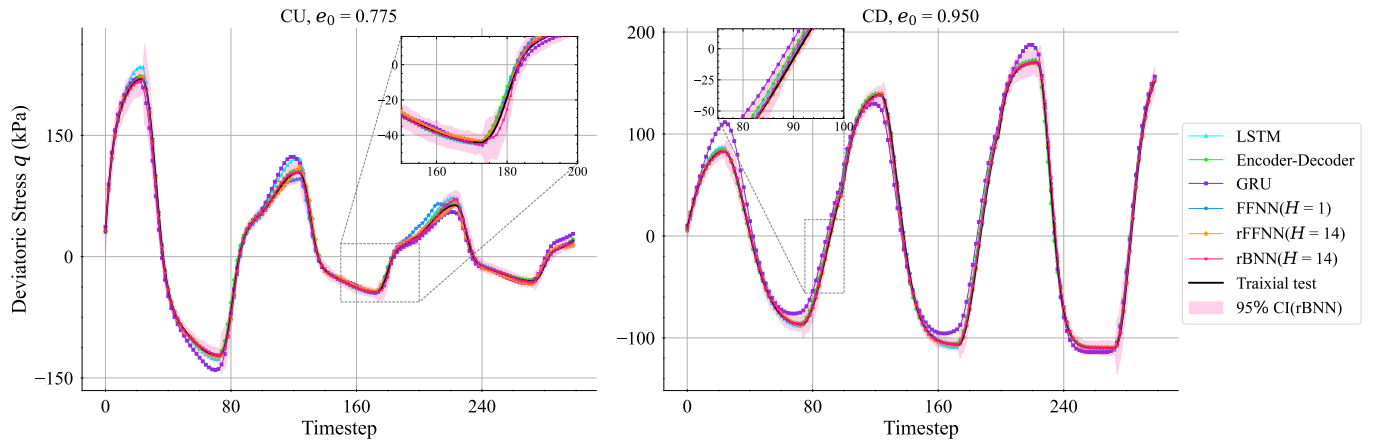


Figure 11: Comparison of model predictions on the test set for **deviatoric stress q** versus timesteps in simulated cyclic triaxial tests. Left panel shows the **undrained test** with initial void ratio $e_0 = 0.775$, and right panel shows the **drained test** with $e_0 = 0.950$.

4.2 Evaluation on experimental data

4.2.1 Monotonic Loading

The laboratory dataset comprises 28 CD triaxial tests on Baskarp sand conducted at Aalborg University [65]. Tests span three initial void ratios ($e_0 = 0.85, 0.70, 0.61$) and nine confining pressures ($\sigma_3 = 5\text{--}800\text{ kPa}$). Soil samples were subjected to axial strains up to maximum values between 12% and 19% of the initial sample height, depending upon the specific test conditions.

For training, $\sim 80\%$ of the data (pressures 20–640 kPa) was used, while 20% at extreme pressures (5 and 800 kPa) formed the test set; validation was performed at 10 kPa. Stress invariants (p, q) and void ratio (e) were normalized following the simulated case (Section 4.1.1). Representative stress–strain curves are shown in Fig. 12.

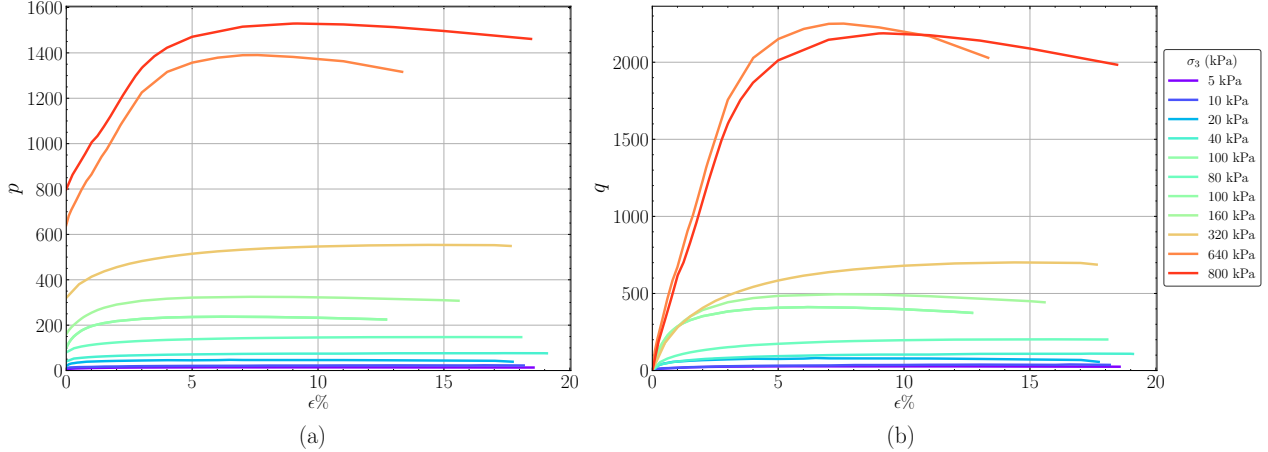


Figure 12: **Representative stress-strain curves** from experimental CD triaxial tests on Baskarp sand specimens done at University of Aalborg ([65]): (a) mean effective stress (p) versus axial strain (ϵ) in %; (b) deviatoric stress (q) versus axial strain (ϵ) in %, illustrating the response under varying confining pressures.

The training process for the experimental dataset followed the methodology outlined for the simulated dataset (Section 4.1.1). Deterministic models (LSTM, GRU, Encoder–Decoder, FFNN, rFFNN) were trained with Huber loss, while rBNN employed the negative ELBO (Eq. (19)). Window length H was tuned using validation; $H = 8$ was optimal for rFFNN and rBNN (Fig. 13). All models employed ReLU activation functions and were trained using the Adam optimizer with learning rate scheduling. For rBNN, Monte Carlo sampling was utilized to propagate parameter uncertainties, enabling confidence intervals for predictions, a feature absent in deterministic models. Architectures are summarized in Table 6.

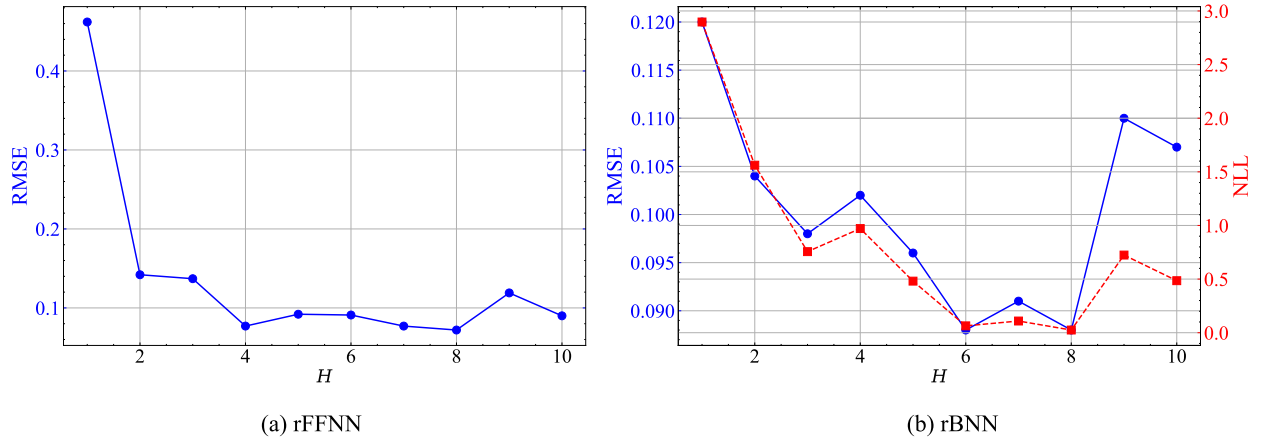


Figure 13: **Selection of H using test set of monotonic experimental case study:** (a) RMSE variation with window length H for rFFNN; (b) RMSE and NLL variation with H for rBNN.

Table 6: Architecture and training configurations for models trained on monotonic experimental data.

Model	Hidden Layers	Neurons/Layer	Training Loss	Activation
LSTM($H=23$)	2	128	Huber	ReLU
Encoder-Decoder($H=23$)	2,2	128(per direction)	Huber	ReLU
GRU($H=23$)	2	128	Huber	ReLU
FFNN ($H=1$)	2	115-110	Huber	ReLU
rFFNN ($H=8$)	2	115-110	Huber	ReLU
rBNN ($H=8$)	2	115-110	– ELBO (Eq. (19))	ReLU

Performance was evaluated with MAE and RMSE, consistent with simulated data. Results (Table 7) show Encoder–Decoder performed best overall for p and q , while rBNN achieved the lowest MAE for e . However, rBNN lagged in p and q , likely due to the limited dataset size inflating posterior uncertainty (Fig. 14). This is in contrast to the simulated dataset, where the larger dataset size (78 tests) allowed the rBNN to perform competitively and produce tighter confidence intervals.

Table 7: **Performance metrics on test set** for DL models trained on experimental monotonic data, with bold values indicating the best performance for each parameter (p , q , e).

Models	p		q		e	
	MAE	RMSE	MAE	RMSE	MAE	RMSE
LSTM($H=23$)	0.0631	0.0801	0.1053	0.1330	0.0298	0.0443
Encoder-Decoder($H=23$)	0.0435	0.0574	0.0598	0.0827	0.0232	0.0293
GRU($H=23$)	0.0767	0.0999	0.1577	0.1887	0.0322	0.0462
FFNN($H=1$)	0.0678	0.0853	0.1064	0.1329	0.0367	0.0508
rFFNN($H=8$)	0.0494	0.0671	0.0754	0.1069	0.0228	0.0336
rBNN($H=8$)	0.0520	0.0720	0.0913	0.1217	0.0194	0.0346

4.2.2 Cyclic Loading

The cyclic loading dataset was taken from [66], consisting of 37 undrained strain-controlled triaxial tests on Ottawa F65 sand. Specimens were prepared using the moist tamping method and consolidated to initial void ratios of 0.576, 0.608, and 0.668, corresponding to relative densities of 75.6%, 63.8%, and 40.0%. Within each group, cyclic stress ratios (CSR (%)) were varied, from 0.040 to 0.140 for $e_0 = 0.668$, 0.050 to 0.220 for $e_0 = 0.608$, and 0.050 to 0.300 for $e_0 = 0.576$ to investigate liquefaction resistance. Liquefaction triggering was defined by reaching an excess pore pressure ratio $r_u = 0.95$.

Data preprocessing followed the same normalization strategy as in Section 4.1.2. For each void ratio group, the lowest and highest CSR tests were held out for testing, the second-highest CSR for validation, and the remainder for training. This structured split enabled the model to learn from a broad range of cyclic stress conditions and soil densities, while allowing for robust evaluation of extrapolation performance.

Deterministic models (LSTM, Encoder-Decoder, GRU, FFNN, rFFNN) were trained with Huber loss, while the rBNN used the negative ELBO loss. Architectures and hyperparameters are summarized in Table 8. Optimal H values were selected using validation performance (Fig. 15), with rBNN employing Monte Carlo sampling for uncertainty quantification.

Table 8: Architecture and training configurations for models trained on cyclic experimental data.

Model	Hidden Layers	Neurons/Layer	Training Loss	Activation
LSTM($H=50$)	2	128	Huber	ReLU
Encoder-Decoder($H=50$)	2,2	128(per direction)	Huber	ReLU
GRU($H=50$)	2	128	Huber	ReLU
FFNN ($H=1$)	3	128	Huber	ReLU
rFFNN ($H=14$)	3	128	Huber	ReLU
rBNN ($H=14$)	2	110	– ELBO (Eq. (19))	ReLU

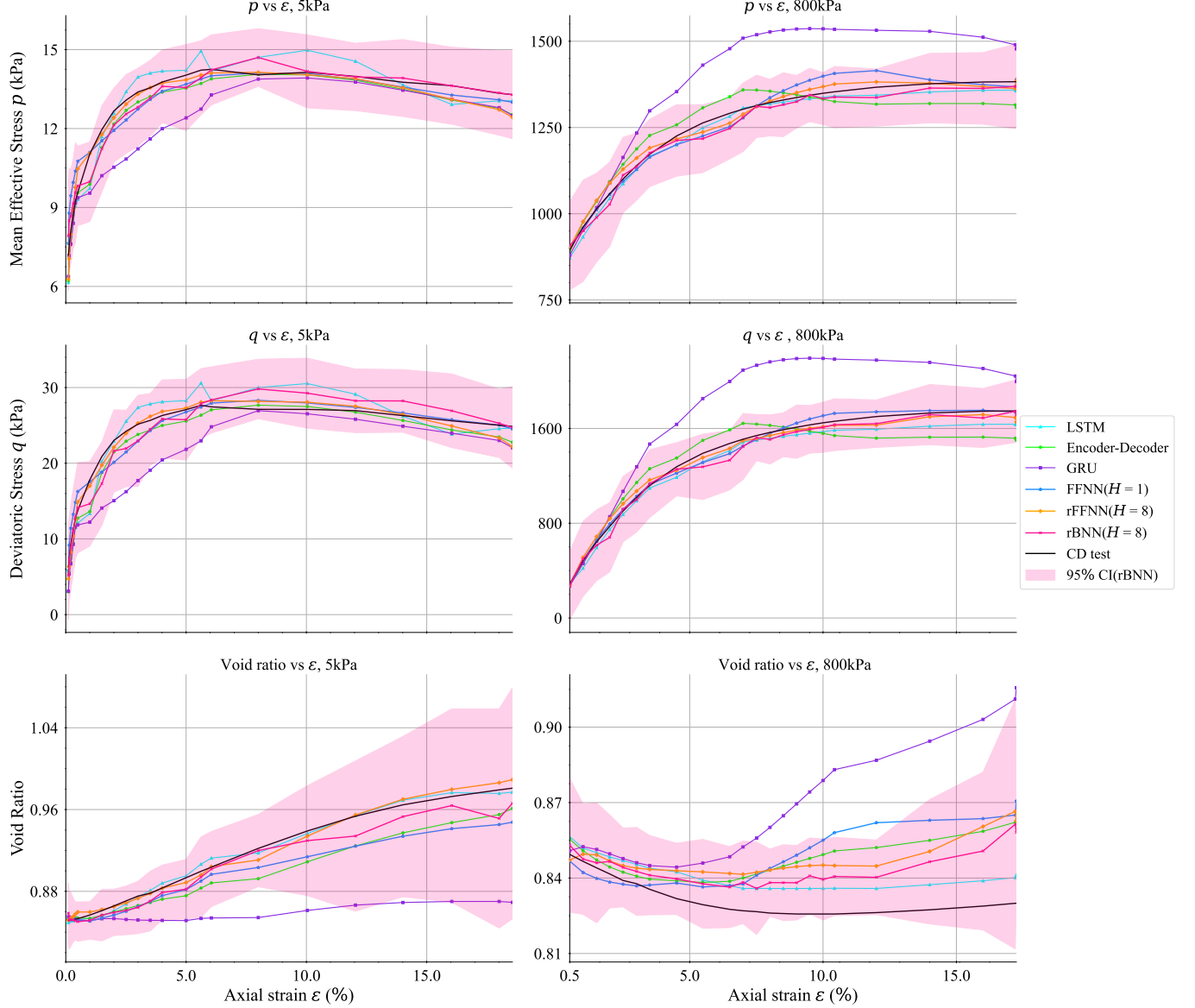


Figure 14: Comparison of model predictions for **mean effective stress (p)**, **deviatoric stress (q)**, and **void ratio** versus **axial strain (ε)** at two extreme confining pressures in experimental CD tests. The left column shows 5 kPa and the right column shows 800 kPa results. Each subplot overlays predictions from various ML models, with the rBNN output including 95% confidence intervals.

The rBNN achieved the best overall performance for p , q , and r_u , closely tracking experimental curves and providing calibrated uncertainty bands (Figs. 16 and 17). Remarkably, these predictions were made using only the initial state variables at $t = 0$ and the prescribed axial strain path, without access to future stress or pore pressure states—a setup that was consistently employed across all test scenarios in this study. Bayesian regularization was especially effective here, as the cyclic setting—with repetitive loading paths—provided richer training signals than the monotonic case, enabling tighter posterior estimates and improved uncertainty quantification. This makes rBNN suitable for capturing complex behaviors like cyclic softening and pore pressure buildup under undrained conditions.

4.3 Computational time

Training was performed on a MacBook Air (M1, 8-core CPU, 7-core GPU) using Python 3.9.19 with TensorFlow 2.15.0 and PyTorch 1.11.0. Training times for simulated and experimental data are shown in Figs. 18a and 18b.

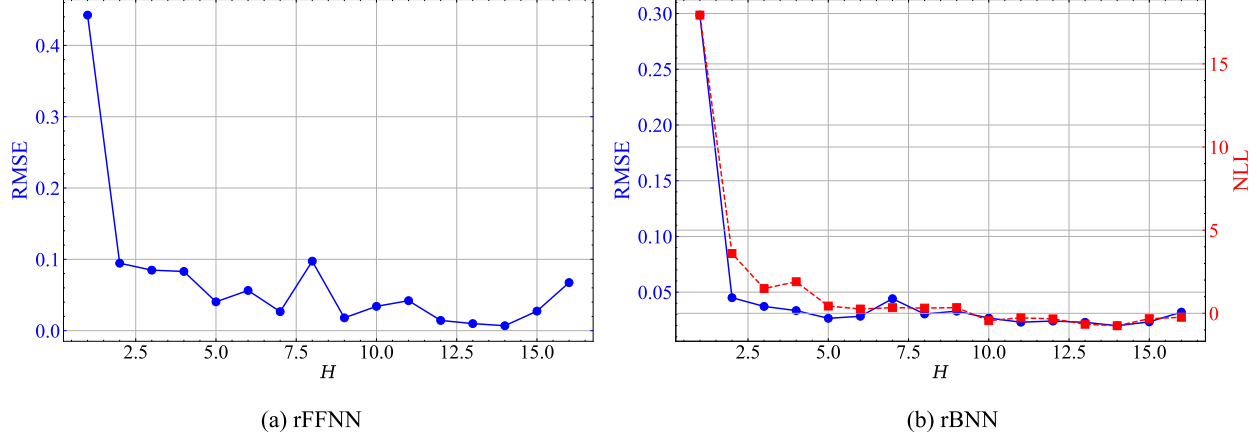


Figure 15: **Selection of H using test set of cyclic experimental case study:** (a) RMSE variation with window length H for rFFNN; (b) RMSE and NLL variation with H for rBNN.

Table 9: **Performance metrics on test set** for DL models trained on experimental cyclic data, with bold values indicating the best performance for each parameter (p , q , r_u).

Models	p		q		r_u	
	MAE	RMSE	MAE	RMSE	MAE	RMSE
LSTM($H = 50$)	0.1104	0.1556	0.1634	0.3836	0.0127	0.0221
Encoder-Decoder ($H = 50$)	0.0820	0.1320	0.1040	0.2270	0.0087	0.0149
GRU($H = 50$)	0.4309	0.7411	0.3738	0.6203	0.0215	0.0368
FFNN ($H = 1$)	0.1402	0.1860	0.1887	0.3122	0.0195	0.0263
rFFNN ($H = 14$)	0.0740	0.1263	0.1205	0.1796	0.0198	0.0301
rBNN ($H = 14$)	0.0718	0.1078	0.0840	0.1427	0.0056	0.0101

Models like LSTMs and Encoder-Decoders had the largest parameter counts (up to $\sim 414k$) due to their recurrent and bidirectional structures, leading to longer per-epoch training compared to rFFNN and rBNN. LSTMs, however, converged efficiently, with modest training times (3.4 and 2.27 minutes on simulated cases). Encoder-Decoders were far costlier, especially on cyclic experimental data (690 minutes), reflecting sensitivity to sequence length and complexity.

In contrast, FFNN and rFFNN trained fastest across datasets. With only 13k–17k parameters, FFNN required under a minute, making it well-suited for rapid deployment.

The rBNN showed more variable behavior. Despite moderate parameter counts, training was slower (7–8 minutes on simulated, up to 120 minutes on experimental cyclic). This stems from Bayesian inference, which uses Monte Carlo sampling and converges more slowly, especially with limited data. However, rBNN uniquely provides predictive uncertainty, absent in deterministic models.

Overall, LSTMs balance efficiency and performance, Encoder-Decoders incur the highest cost in complex settings, FFNNs and rFFNNs excel in low-latency scenarios, and rBNNs trade higher cost for uncertainty quantification — valuable when reliability is critical.

4.4 Key takeaways from performance assessment

The performance evaluation highlights insights from cyclic and monotonic (simulated and experimental) cases, as well as the computational time comparisons. While rBNN is not always the top performer, it consistently provides reliably accurate predictions, often outperforming other models, and uniquely offers predictive uncertainty. Key observations are:

1. Performance across datasets:

- *Monotonic loading (simulated and experimental):* LSTM (simulated) and Encoder-Decoder (experimental) yielded the highest accuracy for stress variables (p , q). rBNN and rFFNN outperformed standard GRU and FFNN in both cases, with rBNN providing the added advantage of uncertainty quantification via

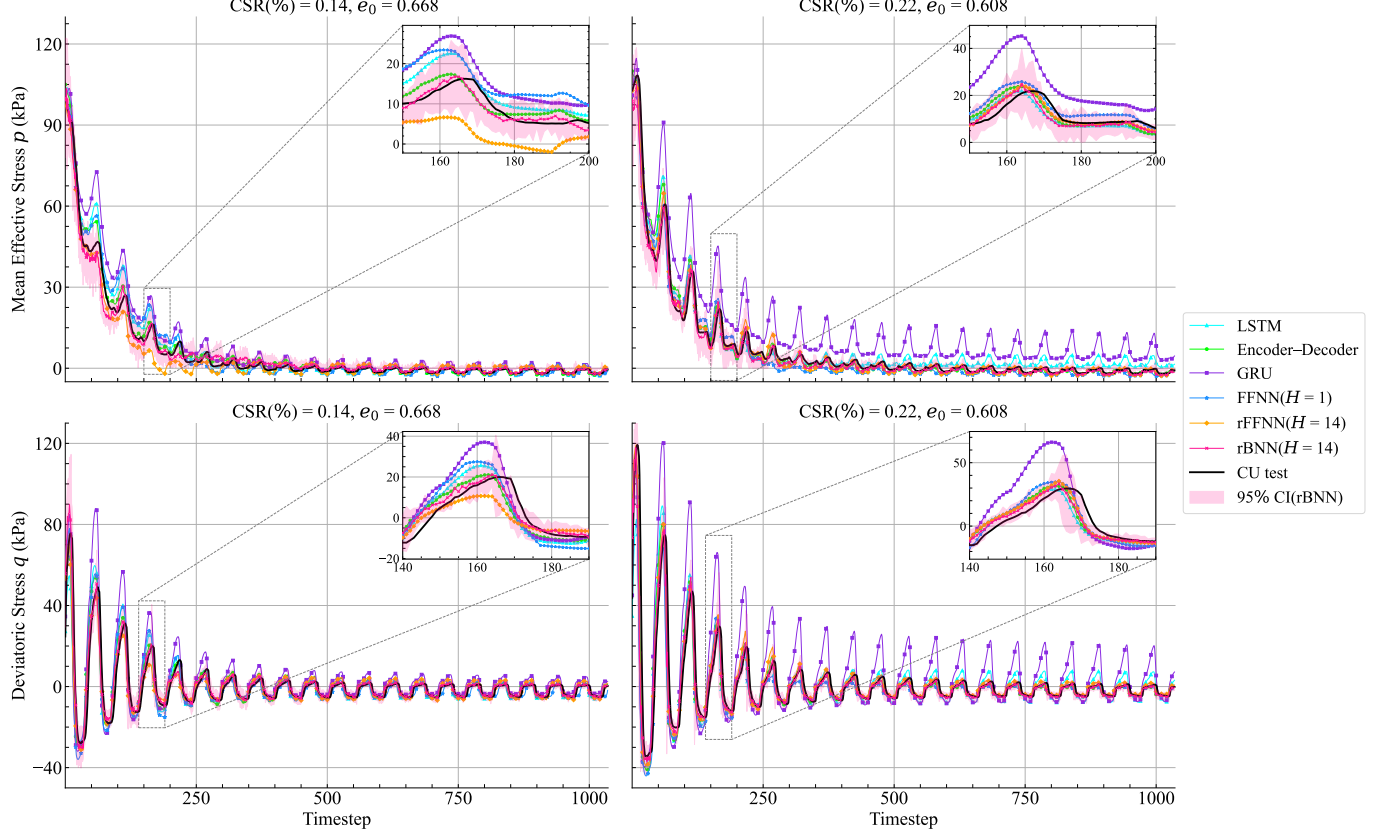


Figure 16: Comparison of model predictions for **mean effective stress** p and **deviatoric stress** q versus timesteps from experimental cyclic undrained tests. Left column shows results for $CSR = 0.14$ and initial void ratio $e_0 = 0.668$, and right column for $CSR = 0.22$ and $e_0 = 0.608$. Each subplot includes predictions from multiple ML models, with the rBNN output displaying 95% confidence intervals.

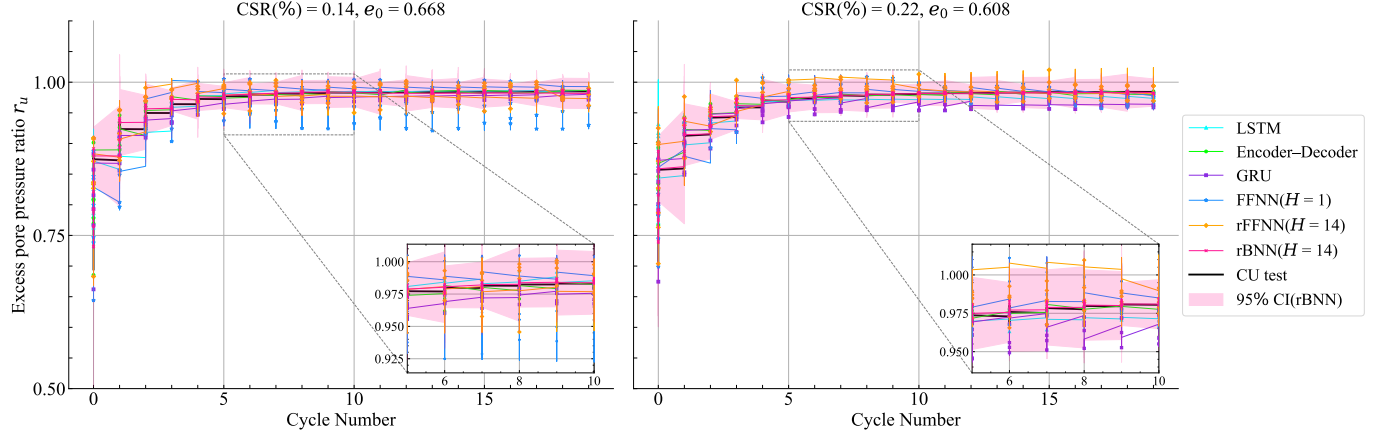


Figure 17: Comparison of model predictions for **excess pore pressure ratio** r_u versus cycle number from experimental cyclic undrained tests. Left column shows results for $CSR = 0.14$ and initial void ratio $e_0 = 0.668$, and right column for $CSR = 0.22$ and $e_0 = 0.608$.

variational inference. Notably, rBNN achieved the best performance for void ratio (e) in the experimental setting, and rFFNN showed consistent robustness despite limited and non-repetitive data.

- *Cyclic loading (simulated and experimental):* rBNN consistently achieved the lowest RMSE and MAE across all state variables—(p, q, ϵ_v) in simulation and (p, q, r_u) in experiments—outperforming all other

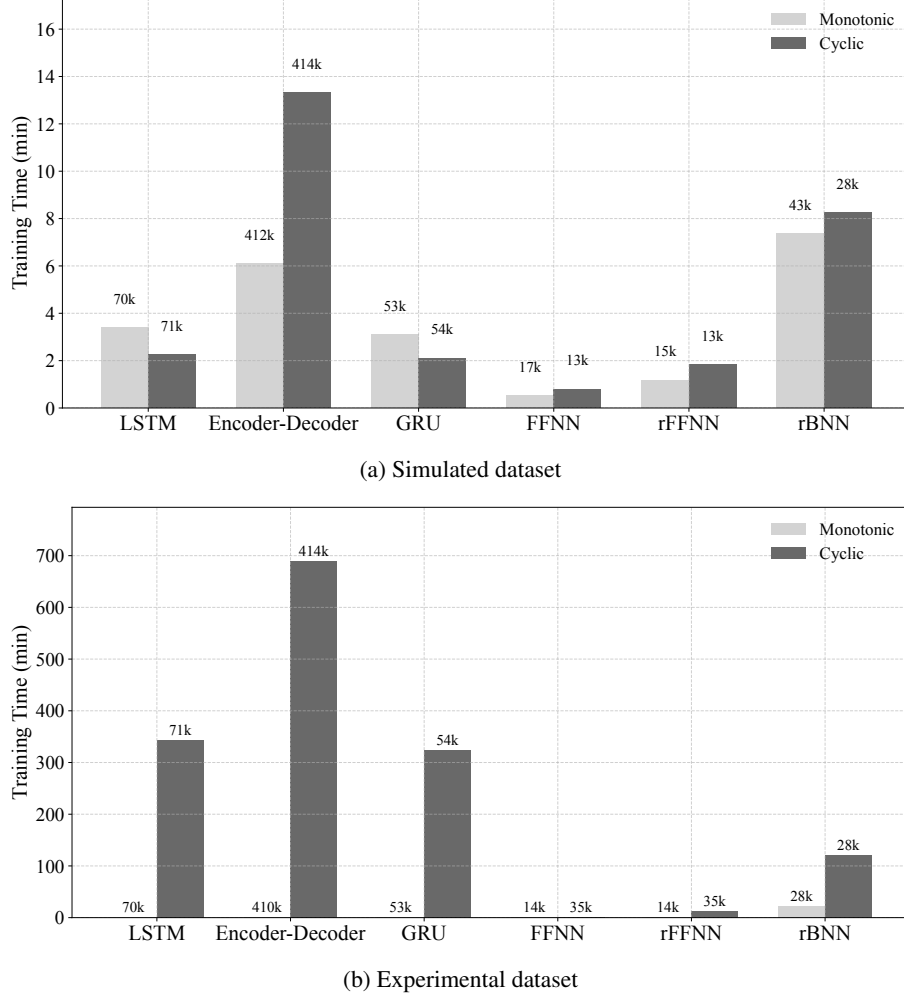


Figure 18: **Comparison of computational training times for different DL models:** (a) models trained on simulated data, and (b) on experimental data. In both subfigures, the model sizes (i.e., the number of parameters) are indicated at the top of each bar in the bar graph.

models. These results indicate that Bayesian regularization benefited from the greater data availability due to longer cyclic loading sequences, leading to improved posterior estimation and well-calibrated probabilistic predictions, in moderate number of overall test samples.

2. **Optimal window length:** rFFNN and rBNN exhibited dataset-dependent optimal window lengths. For monotonic data, best performance occurred at windows ($H = 7-10$), while cyclic data favored longer windows ($H = 14-15$), suggesting that longer input horizons are necessary to fully capture the temporal dependencies and repetitive features present in cyclic stress paths. This highlights the importance of tailoring the input horizon to the nature of loading.
3. **Computational Efficiency:** The rFFNN and rBNN models required significantly fewer trainable parameters compared to LSTMs and Encoder-Decoders. The rFFNN results in faster training times, while rBNN takes longer times due to the sampling framework. The cost of the higher training time is compensated by the output uncertainty provided by the framework.

5 Discussion

This study highlights the potential of recursive neural network architectures, particularly rFFNNs and rBNNs, in modeling the constitutive behavior of sand under both monotonic and cyclic loading conditions. These models emphasize both predictive accuracy and uncertainty quantification. Unlike recurrent models such as LSTMs and GRUs,

which rely on hidden states and gating mechanisms, rFFNNs provide a transparent and interpretable mapping between input features and output states across load steps. This transparency enhances their utility in analyzing the impact of specific input features on the predicted state variables, making rFFNNs and their Bayesian counterpart (rBNNs) valuable tools in geotechnical modeling.

One distinguishing feature of rFFNNs and rBNNs is the use of a sliding window length H , which defines the temporal context for training and recursive predictions. Unlike LSTMs or GRUs, which inherently model sequential dependencies through hidden states that evolve across the full loading sequence, rFFNNs and rBNNs require an explicit window length. The choice of H plays a significant role in balancing predictive performance and computational efficiency, as demonstrated in this study.

From a performance perspective, probabilistic rBNNs outperform other recurrent models, such as LSTMs and Encoder-Decoders, across various metrics for both cyclic simulated and cyclic experimental data. Their simplicity and efficiency allow them to achieve superior accuracy when sufficient training data is available. Additionally, the rBNN provides an essential advantage in uncertainty quantification, producing confidence intervals that account for uncertainties. This feature is particularly beneficial in geotechnical applications where predictive confidence is critical for risk assessment.

On experimental datasets, the inflated confidence intervals observed in monotonic experimental data highlight the challenges posed by data sparsity and measurement noise, as opposed to cyclic experimental datasets where enough data is available. This suggests that the rBNN's probabilistic framework, while robust, requires careful calibration and potentially enhanced priors or noise models to improve its representation of experimental variability in data sparsity.

A promising avenue for future work is the exploration of Bayesian LSTMs. These models combine the sequential modeling capabilities of LSTMs with Bayesian principles, allowing them to handle long-term dependencies while capturing both predictive uncertainties and epistemic uncertainties in model parameters. Bayesian LSTMs could address some of the limitations observed in rBNNs, particularly for experimental datasets where sequential dependencies and noise in measurements play a larger role.

6 Conclusion

This study presents a novel uncertainty-aware recursive Bayesian neural network (rBNN) framework for modeling the stress-strain-volume response of sands under monotonic and cyclic triaxial loading. By enhancing recursive feedforward neural networks (rFFNNs) through a sliding-window training strategy and embedding them within a generalized Bayesian inference framework, the model achieves both high predictive performance and robust uncertainty quantification. The following conclusions are drawn:

The proposed sliding window approach stabilizes training by limiting recursive depth and facilitating localized error correction, enabling better learning of long-range temporal dependencies under cyclic loads. The Bayesian formulation, built upon a deterministic Gaussian output layer and generalized variational inference, introduces principled uncertainty quantification in model predictions while mitigating overfitting.

Comparative evaluations on both simulated and experimental datasets show that the rBNN performs competitively with state-of-the-art deterministic models such as LSTM, GRU, and Encoder–Decoder architectures. While its performance under monotonic loading in simulated cases was comparable but not superior to all baselines, the rBNN demonstrated notable advantages in cyclic scenarios and in providing calibrated uncertainty estimates.

This work establishes a first-of-its-kind probabilistic recursive modeling approach for geomechanics, setting the foundation for future research into fully Bayesian sequence models and their applications in reliability analysis and field-scale monitoring of geomaterials.

CRediT authorship contribution statement

Toiba Noor: Conceptualization, Methodology, Software, Writing - original draft. **Soban Nasir Lone:** Methodology. **G.V. Ramana:** Supervision, Writing - review & editing. **Rajdip Nayek:** Conceptualization, Supervision, Methodology, Writing - review & editing.

Declaration of Competing Interest

The authors declare that they have no known competing financial interests or personal relationships that could have appeared to influence the work reported in this paper.

Data Availability

Some or all data, models, or code that support the findings of this study are available from the corresponding author upon reasonable request.

Acknowledgements

T. Noor acknowledges the financial support received from the Prime Minister's Research Fellowship (PMRF) and **R. Nayek** acknowledges the financial support received from ANRF (vide grant no. SRG/2022/001410), Ministry of Shipping, Ports, and Waterways, and the matching grant from IIT Delhi.

A Training and Optimization of RNNs

The data normalization process for RNNs mirrors the approach used for rFFNN and rBNN. Models across the RNN family, including LSTM, Encoder-Decoder, and GRU, utilize the same data preparation strategy for both simulated and experimental datasets. The RNN models were trained using input data structured as shown in Fig. 19. RNNs maintain an internal **hidden state** that acts as a memory of past inputs. For each instance m and at each time step t , the current hidden state, $\mathbf{s}_t^{*(m)}$, is computed as a function of the previous hidden state, $\mathbf{s}_{t-1}^{*(m)}$, the current input, $\mathbf{u}_t^{(m)}$, and the model's trainable parameters, $\theta^{(m)}$. This feedback mechanism is described by:

$$\begin{pmatrix} \mathbf{s}_0^{(1)} & \mathbf{u}_1^{(1)} & \theta^{(1)} & \dots & \mathbf{s}_{N-1}^{(1)} & \mathbf{u}_N^{(1)} & \theta^{(1)} \\ \mathbf{s}_0^{(2)} & \mathbf{u}_1^{(2)} & \theta^{(2)} & \dots & \mathbf{s}_{N-1}^{(2)} & \mathbf{u}_N^{(2)} & \theta^{(2)} \\ \vdots & & & & & & \\ \mathbf{s}_0^{(M)} & \mathbf{u}_1^{(M)} & \theta^{(M)} & \dots & \mathbf{s}_{N-1}^{(M)} & \mathbf{u}_N^{(M)} & \theta^{(M)} \end{pmatrix} \rightarrow \begin{pmatrix} \mathbf{s}_N^{(1)} \\ \mathbf{s}_N^{(2)} \\ \vdots \\ \mathbf{s}_N^{(M)} \end{pmatrix}$$

Figure 19: Illustration of the data structure used for Recurrent Neural Networks.

$$\mathbf{s}_t^{*(m)} = f(\mathbf{s}_{t-1}^{*(m)}, \mathbf{u}_t^{(m)}, \theta^{(m)}) \quad (34)$$

During training, the RNNs process the entire available loading sequence incrementally. At each strain increment, the hidden state from the preceding time step is propagated forward and integrated with the current input to update the model's internal memory. Losses are then calculated for the predictions made at each of these increments, strictly adhering to this sequential feedback framework, ensuring the hidden state effectively encapsulates all temporal dependencies accumulated up to that point.

For simulated data, hyperparameters of each RNN model were systematically tuned to achieve optimal performance in the validation set. The hyperparameter space for LSTM included learning rates (0.0001 to 0.01), number of LSTM layers (1 to 4), and number of nodes in each layer (50 to 200). Batch sizes (1 to 25) were validated to balance computational efficiency and gradient stability. The suitability of the Huber loss function over MSE loss was evaluated based on validation loss. Optimization algorithms, including Adam and RMSprop, were also validated. The number of epochs ranged from 1000 – 10000, and model selection was guided by Total MSE of the validation set. A similar systematic approach was applied for Encoder-Decoder and GRU models, with final details of the architecture summarized in Tables 1, 4, 6 and 8

References

- [1] Yi Hong, Chi Hung Koo, Chao Zhou, Charles WW Ng, and LZ Wang. Small strain path-dependent stiffness of Toyoura sand: Laboratory measurement and numerical implementation. *International Journal of Geomechanics*, 17(1):1–10, 2017.
- [2] Zhen-Yu Yin, Pierre-Yves Hicher, Christophe Dano, and Yin-Fu Jin. Modeling mechanical behavior of very coarse granular materials. *Journal of Engineering Mechanics*, 143(1), 2017.
- [3] Kenji Ishihara. *Soil behaviour in earthquake geotechnics*. Oxford University Press, 1996.

- [4] Yousef Hejazi, Daniel Dias, and Richard Kastner. Impact of constitutive models on the numerical analysis of underground constructions. *Acta Geotechnica*, 3:251–258, 2008.
- [5] Marco M Secondi, Giovanni Crosta, Claudio di Prisco, Gabriele Frigerio, Paolo Frattini, and Federico Agliardi. Landslide motion forecasting by a dynamic visco-plastic model. *Landslide Science and Practice: Volume 3: Spatial Analysis and Modelling*, pages 151–159, 2013.
- [6] Mark Randolph and Susan Gourvenec. *Offshore geotechnical engineering*. CRC press, 2017.
- [7] Daniel Charles Drucker and William Prager. Soil mechanics and plastic analysis or limit design. *Quarterly of Applied Mathematics*, 10(2):157–165, 1952.
- [8] Nicos Makris and MC Constantinou. Models of viscoelasticity with complex-order derivatives. *Journal of Engineering Mechanics*, 119(7):1453–1464, 1993.
- [9] Yang-Ping Yao, Lin Liu, Ting Luo, Yu Tian, and Jian-Min Zhang. Unified hardening model for clays and sands. *Computers and Geotechnics*, 110:326–343, 2019.
- [10] G Cassiani, A Brovelli, and T Hueckel. A strain-rate-dependent modified Cam-Clay model for the simulation of soil/rock compaction. *Geomechanics for Energy and the Environment*, 11:42–51, 2017.
- [11] Michael G Katona. Evaluation of viscoplastic cap model. *Journal of Geotechnical Engineering*, 110(8):1106–1125, 1984.
- [12] Y. F. Dafalias. *On elastoplastic-viscoplastic constitutive modelling of cohesive soils*, page 16. Routledge, 1st edition, 1986. ISBN 9780203753583.
- [13] Zhen-Yu Yin, Pierre-Yves Hicher, Yin-Fu Jin, Zhen-Yu Yin, Pierre-Yves Hicher, and Yin-Fu Jin. Elastoplastic modeling of soils: From Mohr-Coulomb to SIMSAND. *Practice of Constitutive Modelling for Saturated Soils*, pages 121–176, 2020.
- [14] Zhen Yu Yin and Yin Fu Jin. *Practice of optimisation theory in geotechnical engineering*. Springer Singapore, Singapore, April 2019. ISBN 9789811334078. Publisher Copyright: © 2022 Springer Nature Switzerland AG. Part of Springer Nature.
- [15] Ivo Herle. Fundamentals of constitutive modelling for soils. *ALERT Doctoral School 2021 Constitutive Modelling in Geomaterials*, page 3, 2021.
- [16] T Schanz and PA Vermeer. Angles of friction and dilatancy of sand. *Géotechnique*, 46(1):145–151, 1996.
- [17] Jinglin Yang and XS Li. State-dependent strength of sands from the perspective of unified modeling. *Journal of Geotechnical and Geoenvironmental Engineering*, 130(2):186–198, 2004.
- [18] Wei Wu. Rational approach to anisotropy of sand. *International Journal for Numerical and Analytical Methods in Geomechanics*, 22(11):921–940, 1998.
- [19] Jamshid Ghaboussi, JH Garrett Jr, and Xiping Wu. Knowledge-based modeling of material behavior with neural networks. *Journal of Engineering Mechanics*, 117(1):132–153, 1991.
- [20] Glenn W Ellis, Chengwan Yao, and Rongda Zhao. Neural network modeling of the mechanical behavior of sand. In *Engineering Mechanics*, pages 421–424. ASCE, 1992.
- [21] GW Ellis, C Yao, Rui Zhao, and Df Penumadu. Stress-strain modeling of sands using artificial neural networks. *Journal of Geotechnical Engineering*, 121(5):429–435, 1995.
- [22] DE Sidarta and J Ghaboussi. Constitutive modeling of geomaterials from non-uniform material tests. *Computers and Geotechnics*, 22(1):53–71, 1998.
- [23] Dayakar Penumadu and Rongda Zhao. Triaxial compression behavior of sand and gravel using artificial neural networks. *Computers and Geotechnics*, 24(3):207–230, 1999.
- [24] Ghassem Habibagahi and Alireza Bamdad. A neural network framework for mechanical behavior of unsaturated soils. *Canadian Geotechnical Journal*, 40(3):684–693, 2003.
- [25] Yacoub Najjar and Xiaobin" Carol" Zhang. Characterizing the 3D stress-strain behavior of sandy soils: A neuro-mechanistic approach. In *Numerical methods in Geotechnical Engineering*, volume 24, pages 43–57. Elsevier, 2000.
- [26] Jamshid Ghaboussi and Djoni Eka Sidarta. New nested adaptive neural networks for constitutive modeling. *Computers and Geotechnics*, 22(1):29–52, 1998.
- [27] Imad A Basheer. Selection of methodology for neural network modeling of constitutive hystereses behavior of soils. *Computer-Aided Civil and Infrastructure Engineering*, 15(6):445–463, 2000.

- [28] Yoshua Bengio, Patrice Simard, and Paolo Frasconi. Learning long-term dependencies with gradient descent is difficult. *IEEE transactions on neural networks*, 5(2):157–166, 1994.
- [29] Samy Bengio, Oriol Vinyals, Navdeep Jaitly, and Noam Shazeer. Scheduled sampling for sequence prediction with recurrent neural networks. In *Proceedings of the 29th International Conference on Neural Information Processing Systems - Volume 1*, NIPS’15, page 1171–1179, Cambridge, MA, USA, 2015. MIT Press.
- [30] Jian-Hua Zhu, Musharraf M Zaman, and Scott A Anderson. Modeling of soil behavior with a recurrent neural network. *Canadian Geotechnical Journal*, 35(5):858–872, 1998.
- [31] YM Najjar and HE Ali. Simulating the stress-strain behavior of Nevada sand by Artificial Neural Networks. In *Proceedings of the 5th US National Congress on Computational Mechanics (USACM), Boulder, Colorado*, pages 0–1, 1999.
- [32] Miguel P Romo, Silvia R García, Manuel J Mendoza, and Victor Taboada-Urtzuástegui. Recurrent and constructive-algorithm networks for sand behavior modeling. *International Journal of Geomechanics*, 1(4):371–387, 2001.
- [33] Sepp Hochreiter and Jürgen Schmidhuber. Long short-term memory. *Neural Computation*, 9(8):1735–1780, 1997.
- [34] Junyoung Chung, Caglar Gulcehre, Kyunghyun Cho, and Yoshua Bengio. Empirical evaluation of gated recurrent neural networks on sequence modeling. In *NIPS 2014 Workshop on Deep Learning, December*, page 4436, 2014.
- [35] Pin Zhang, Zhen-Yu Yin, and Yin-Fu Jin. State-of-the-art review of machine learning applications in constitutive modeling of soils. *Archives of Computational Methods in Engineering*, pages 1–26, 2021.
- [36] Ning Zhang, Shui-Long Shen, Annan Zhou, and Yin-Fu Jin. Application of LSTM approach for modelling stress–strain behaviour of soil. *Applied Soft Computing*, 100:106959, 2021.
- [37] Tongming Qu, Shaocheng Di, YT Feng, Min Wang, Tingting Zhao, and Mengqi Wang. Deep learning predicts stress–strain relations of granular materials based on triaxial testing data. *Computer Modeling in Engineering & Sciences*, 128(1):129–144, 2021.
- [38] Mengmeng Wu, Zhangqi Xia, and Jianfeng Wang. Constitutive modelling of idealised granular materials using machine learning method. *Journal of Rock Mechanics and Geotechnical Engineering*, 15(4):1038–1051, 2023.
- [39] Pin Zhang, Zhen-Yu Yin, Yin-Fu Jin, Jie Yang, and Brian Sheil. Physics-informed multifidelity residual neural networks for hydromechanical modeling of granular soils and foundation considering internal erosion. *Journal of Engineering Mechanics*, 148(4):04022015, 2022.
- [40] Pin Zhang, Zhen-Yu Yin, Yin-Fu Jin, and Guan-Lin Ye. An AI-based model for describing cyclic characteristics of granular materials. *International Journal for Numerical and Analytical Methods in Geomechanics*, 44(9):1315–1335, 2020.
- [41] Kaushik Jas, Amalesh Jana, and G. R. Dodagoudar. Prediction of shear strain and excess pore water pressure response in liquefiable sands under cyclic loading using deep learning model. *Japanese Geotechnical Society Special Publication*, 10(46):1729–1734, 2024.
- [42] Omer Tugsad Birinci, Mehmet Baris Can Ulker, and Gulsen Taskin Kaya. Prediction of pore water pressure generation of liquefiable clean sands under cyclic shear loading through deep learning. *Geomechanics and Geoengineering*, pages 1–22, 2025.
- [43] Kyunghyun Cho, Bart Van Merriënboer, Caglar Gulcehre, Dzmitry Bahdanau, Fethi Bougares, Holger Schwenk, and Yoshua Bengio. Learning phrase representations using rnn encoder-decoder for statistical machine translation. *arXiv preprint arXiv:1406.1078*, 2014.
- [44] Shengdong Du, Tianrui Li, Yan Yang, and Shi-Jinn Horng. Multivariate time series forecasting via attention-based encoder-decoder framework. *Neurocomputing*, 388:269–279, 2020.
- [45] David JC MacKay. Probable networks and plausible predictions- A review of practical Bayesian methods for supervised neural networks. *Network: Computation in Neural Systems*, 6(3):469, 1995.
- [46] Radford M Neal. *Bayesian learning for neural networks*, volume 118. Springer Science & Business Media, 2012.
- [47] Laurent Valentin Jospin, Hamid Laga, Farid Boussaid, Wray Buntine, and Mohammed Bennamoun. Hands-on Bayesian neural networks—A tutorial for deep learning users. *IEEE Computational Intelligence Magazine*, 17(2):29–48, 2022.
- [48] Jeremias Knoblauch, Jack Jewson, and Theodoros Damoulas. An optimization-centric view on Bayes’ rule: Reviewing and generalizing variational inference. *Journal of Machine Learning Research*, 23(132):1–109, 2022. URL <http://jmlr.org/papers/v23/19-1047.html>.

- [49] Abhik Ghosh and Ayanendranath Basu. Robust Bayes estimation using the density power divergence. *Annals of the Institute of Statistical Mathematics*, 68:413–437, 2016.
- [50] Benjamin Guedj. A primer on pac-Bayesian learning. *arXiv preprint arXiv:1901.05353*, 2019.
- [51] Khanh Pham, Sanghoon Jung, Sangyeong Park, Dongku Kim, and Hangseok Choi. Bayesian neural network for estimating stress-strain behaviors of frozen sand. *KSCE Journal of Civil Engineering*, 26(2):933–941, 2022.
- [52] Yarin Gal and Zoubin Ghahramani. Dropout as a Bayesian approximation: Representing model uncertainty in deep learning. In *International Conference on Machine Learning*, pages 1050–1059. PMLR, 2016.
- [53] Pin Zhang, Zhen-Yu Yin, and Brian Sheil. Interpretable data-driven constitutive modelling of soils with sparse data. *Computers and Geotechnics*, 160:105511, 2023.
- [54] Vincent Fortuin. Priors in Bayesian deep learning: A review. *International Statistical Review*, 90(3):563–591, 2022.
- [55] Takuo Matsubara, Jeremias Knoblauch, François-Xavier Briol, and Chris J Oates. Robust generalised Bayesian inference for intractable likelihoods. *Journal of the Royal Statistical Society Series B: Statistical Methodology*, 84(3):997–1022, 2022.
- [56] Alp Kucukelbir, Dustin Tran, Rajesh Ranganath, Andrew Gelman, and David M Blei. Automatic differentiation variational inference. *Journal of Machine Learning Research*, 18(14):1–45, 2017.
- [57] Diederik P Kingma. Auto-encoding variational bayes. *arXiv preprint arXiv:1312.6114*, 2013.
- [58] Charles Blundell, Julien Cornebise, Koray Kavukcuoglu, and Daan Wierstra. Weight uncertainty in neural network. In *International Conference on Machine Learning*, pages 1613–1622. PMLR, 2015.
- [59] Jeremias Knoblauch, Jack Jewson, and Theodoros Damoulas. Generalized variational inference: Three arguments for deriving new posteriors. *arXiv preprint arXiv:1904.02063*, 2019.
- [60] T Schanz, PA Vermeer, and P Gc Bonnier. The hardening soil model: Formulation and Verification. *Beyond 2000 in Computational Geotechnics*, 1:281–296, 1999.
- [61] T Wichtmann, I Kimmig, and T Triantafyllidis. On correlations between “dynamic”(small-strain) and “static”(large-strain) stiffness moduli—An experimental investigation on 19 sands and gravels. *Soil Dynamics and Earthquake Engineering*, 98:72–83, 2017.
- [62] Joshua V Dillon, Ian Langmore, Dustin Tran, Eugene Brevdo, Srinivas Vasudevan, Dave Moore, Brian Patton, Alex Alemi, Matt Hoffman, and Rif A Saurous. Tensorflow distributions. *arXiv preprint arXiv:1711.10604*, 2017.
- [63] Iyad Alkroosh and Hamid Nikraz. Predicting axial capacity of driven piles in cohesive soils using intelligent computing. *Engineering Applications of Artificial Intelligence*, 25(3):618–627, 2012.
- [64] Zhen-Yu Yin, Ze-Xiang Wu, and Pierre-Yves Hicher. Modeling monotonic and cyclic behavior of granular materials by exponential constitutive function. *Journal of engineering mechanics*, 144(4):04018014, 2018.
- [65] Lars Bo Ibsen and Lars Bødker Bødker. Baskarp sand no. 15: Data report 9301. *Aalborg: Geotechnical Engineering Group. Data Report, No. 9401*, 1994.
- [66] Mohamed A ElGhoraiby, Hanna Park, and Majid T Manzari. Stress-strain behavior and liquefaction strength characteristics of Ottawa F65 sand. *Soil Dynamics and Earthquake Engineering*, 138:106292, 2020.